First-principles study of metal-semiconductor contacts and quantum transport simulations for 5.1-nm monolayer $MoSi_2N_4$ devices

Zhanhai Li, Jianing Han, Shengguo Cao, Zhenhua Zhang,* and Xiaoqing Deng†
Hunan Provincial Key Laboratory of Flexible Electronic Materials Genome Engineering, Changsha University of Science and Technology, Changsha 410114, China

(Received 17 February 2024; revised 2 May 2024; accepted 6 May 2024; published 30 May 2024)

The semiconductor industry has been facing obstacles in designing low-power (LP) nanoelectronic devices due to the lack of accurate theoretical simulations and low-resistance contacts of heterojunctions. Here, based on experimental data, we discover that the generalized gradient approximation using the Fritz Haber Institute pseudopotential accurately describes the lattice constants and electronic properties of monolayer $MoSi_2N_4$. It is further confirmed that this method is also applicable to characterize the electrical contact properties and device transport characteristics of metal/$MoSi_2N_4$ heterojunctions (where metal includes Sc, Bi, Ag, Al, Ti, graphene, Cr, Fe, Cu, Co, Au, Pd, Ni, and Pt). Calculations show that various bulk metal/$MoSi_2N_4$ heterojunctions exhibit *n*-type Schottky barrier contact features, and it is possible to achieve 100% carrier injection for $MoSi_2N_4$ with Sc, Ag, Ti, Pd, and Pt contacts. Using the Schottky-Mott rule and quantum transport simulation, a strong Fermi-level pinning effect at the metal/$MoSi_2N_4$ interfaces is observed, and Sc is identified as the best metal electrode. The 5.1-nm *p-i-n* field-effect transistor (FET) with Sc electrodes can meet the OFF-state current requirement of the 2013 International Technology Roadmap for Semiconductors standard for high-performance and LP FET devices. By employing a high-*k* gate, the ON-state current for the undoped LP device can be improved by 2 orders of magnitude, and its high ON:OFF ratio is up to 3×10^6. These findings provide insights into the metal/$MoSi_2N_4$ interface behaviors and provide a theoretical reference for designing $MoSi_2N_4$-based nanoelectronic devices by selecting suitable electrodes with low contact resistance.

DOI: 10.1103/PhysRevApplied.21.054062

I. INTRODUCTION

In short-channel devices, carrier transport is nearly ballistic and almost all power dissipation occurs at the metal-semiconductor interface [1]. Therefore, optimizing the contact behavior between metal electrodes and channel semiconductor materials becomes a crucial issue. However, owing to the susceptibility of atomic-thickness two-dimensional (2D) semiconductor materials to interface traps, lattice defects, metal diffusion, and covalent bonding, which are induced by high-energy metal-deposition processes [2], the Fermi-level pinning (FLP) effect and significant Schottky barrier at the metal-semiconductor interface are always present [3,4]. To mitigate the impact of interface states, various strategies [5–7], such as using hexagonal boron nitride or graphene interlayers [8–11], introducing buffer layers [12], organic doping [13], low-work-function metals [14], phase engineering [15], etc., have been proposed. However, the interlayers and buffer layers introduce additional van der Waals (vdW) gaps that create more tunneling barriers, hindering effective carrier injection [16]. Moreover, these strategies are not yet scalable for industrial applications, and are primarily focused on multilayer MoS_2 [17]. Fortunately, direct metal contact has been recently reported as an effective alternative method for injecting carriers into 2D semiconductor transistors [18]. Multiple experimental studies have proposed assembly techniques that preserve the perfect cleanliness of the contact region without damaging the fine lattice of the interface [19–23].

In addition to external factors, the semiconductor channel material itself is a crucial factor determining device performance. However, a large number of theoretical predictions and experimental reports on field-effect transistors (FETs) prove that there are few 2D semiconductor materials that are suitable as their channels. For instance, black phosphorus [24] and InSe [25] are prone to chemical degradation and corrosion in the environment. MoS_2 [26] oxidizes in humid air below 373 K. Rarity hinders the large-scale production of arsenene [27], antimonene [28], and tellurene [29]. Recently, a 2D monolayer $MoSi_2N_4$ with excellent thermal, mechanical, electronic, and metal contact properties and environmental stability has been successfully fabricated [30–38]. Its optical band gap is 1.94 eV, and its electron (hole) mobility is 270 $cm^2\ V^{-1}\ s^{-1}$

*Corresponding author: zhzhang@csust.edu.cn
†Corresponding author: xq_deng@163.com

 © 2024 American Physical Society

(1200 cm^2 V^{-1} s^{-1}), 3 times (5 times) larger than that of MoS_2 [39]. It holds significant potential for ideal electrical contacts [40–42] and sub-5-nm node transistors [43–45]. However, to our knowledge, there are currently no reports on accurate theoretical calculations for the band gap and lattice constant of the $MoSi_2N_4$ monolayer, and the values of 1.74 eV for the band gap and 2.91 Å for the lattice constant, which have usually been used in previous theoretical studies, were obtained using the Perdew-Burke-Ernzerhof (PBE) functional in the generalized gradient approximation (GGA). Although they are closer to experimental values than those from the hybrid functional Heyd-Scuseria-Ernzerhof (HSE06) calculation, there are still errors of 10.31% and 1.02% in the gap and lattice constant values. The severe underestimation of the gap leads to the underestimation of the Schottky barrier height (SBH) for metal-semiconductor contacts; even realistic Schottky contacts are regarded as Ohmic contacts, giving rise to an overestimation of $MoSi_2N_4$-based device performance in quantum transport simulations. Therefore, using a theoretical calculation method that can accurately predict experimental measurements is crucial to in-depth explorations of the electrical contact and transport features for the monolayer $MoSi_2N_4$/metal interface.

In this work, by checking 15 different combinations of computing methods, we identify the most suitable one, the GGA using the Fritz Haber Institute (FHI) pseudopotential, which can accurately describe the band gap and lattice constant for the $MoSi_2N_4$ monolayer. Using such a method, we investigate the electrical contact properties of 14 different metal/$MoSi_2N_4$ heterojunctions. The result reveals a strong coupling with a significant FLP effect occurring at the bulk metal/$MoSi_2N_4$ interface. In contrast, the graphene/$MoSi_2N_4$ interface can eliminate FLP due to the weak vdW force. By calculating the tunneling probability, interface SBH, and transport gap, we find that Sc and Cr are the most suitable electrode materials for $MoSi_2N_4$-based FETs among all bulk metals. Subsequently, based on the 2013 International Technology Roadmap for Semiconductors (ITRS) standards [46], we evaluate the performance of 5.1-nm FETs with Sc and Cr electrodes and $MoSi_2N_4$ as the channel material by using quantum transport simulations, and the main factors influencing device performance are clarified by the calculated device transmission spectra, projected local density of states (PLDOS), spectral current, and local density of states (LDOS). These findings gain theoretical insight into the metal/$MoSi_2N_4$ interface behaviors and provide a theoretical reference for designing 2D $MoSi_2N_4$-based high-performance (HP) nanoelectronic devices.

II. METHODS

All calculations are performed using the first-principles calculation software package ATOMISTIX TOOLKIT based on density-functional theory (DFT) combined with the nonequilibrium Green's function technique [47,48]. The PBE GGA is employed to describe exchange-correlation effects [49], and the electronic wave functions are expanded by the linear combination of atomic orbitals for the double zeta polarized (DZP) basis set [50,51], with the FHI pseudopotential. It is noted that Fe, Co, and Ni metal contacts are inherently spin-polarized, and their initial magnetic state is set to ferromagnetic for calculations. To achieve a balance between computational efficiency and accuracy, the density grid cutoff is set to 160 hartree. The Brillouin zone sampling Monkhorst-Pack grids [52] are set to $27 \times 1 \times 27$ and $27 \times 1 \times 186$ in the x, y, and z axis directions for the unit cell and device, respectively. The convergence criteria for the self-consistent field and atomic Herman-Feynman forces are set to 10^{-5} eV and 10^{-2} eV/Å, respectively. A vacuum layer of 3 nm in the z axis direction is introduced to eliminate interactions between the model and periodic images. Additionally, Grimme's zero-damping DFT-D3 method [53] is applied to correct vdW interactions, and a dipole correction is used to eliminate the pseudointeraction caused by the periodicity in the z direction. For simplicity, the Fermi level is set to zero for calculations.

The Landauer-Büttiker formula is employed to calculate the drain-source current (I_{ds}) under a given bias voltage (V_{b}) and gate voltage (V_{g}) as follows:

$$I_{\mathrm{ds}}(V_{\mathrm{b}}, V_{\mathrm{g}}) = \frac{2e}{h} \int_{-\infty}^{+\infty} T(E, V_{\mathrm{b}}, V_{\mathrm{g}})[f_d(E-\mu_d) - f_s(E-\mu_s)]dE, \quad (1)$$

where $T(E,\ V_{\mathrm{b}},\ V_{\mathrm{g}})$ is the transmission probability at the given bias and gate voltages, and $f_{s(d)}$ and $\mu_{s(d)}$ are the Fermi-Dirac distribution function and electrochemical potential for the source (drain) electrode.

The transmission coefficient $T(E,k_x)$ for a given k_x and energy E is calculated by

$$T(E,k_x) = \mathrm{Tr}[G^r(E,k_x) \cdot \Gamma_s(E,k_x) \cdot G^a(E,k_x) \cdot \Gamma_d(E,k_x)], \quad (2)$$

where $\mathrm{G}^{r(a)}(E,k_x)$ represents the retarded (advanced) Green's function, $\Gamma_{s(d)}(E,k_x) = i\left[\sum_{s(d)}^{r}(E,k_x) - \sum_{s(d)}^{a}(E,k_x)\right]$ is the source (drain) electrode-induced level broadening described by the electrode self-energy $\sum_{s(d)}^{r(a)}(E,k_x)$, reflecting the influence of the electrodes on the scattering region [54].

III. RESULTS AND DISCUSSION

A. Electronic properties of monolayer $MoSi_2N_4$

The atomic structure of $MoSi_2N_4$ and its side and top views are illustrated in Figs. 1(a)–1(c), respectively. It

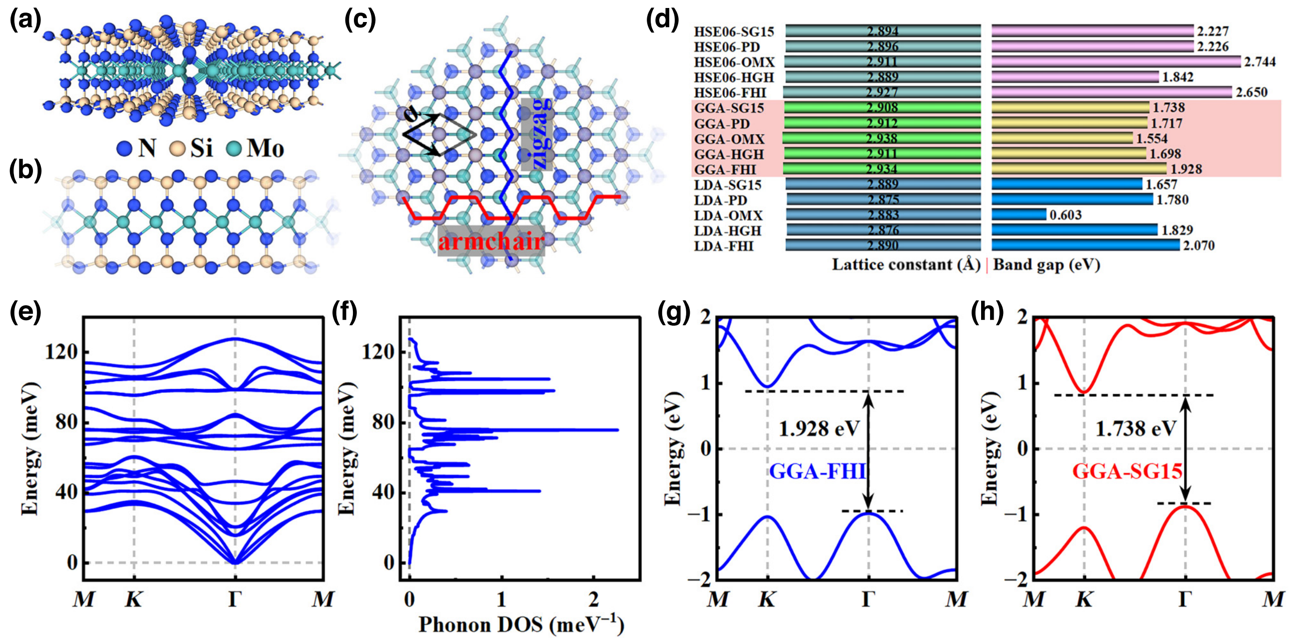

FIG. 1. (a) The atomic structure of the $MoSi_2N_4$ monolayer, (b) side view, and (c) top view. (d) Lattice constant and band gap of fully relaxed $MoSi_2N_4$ crystal obtained by employing 15 different computational methods. (e) Phonon spectrum, and (f) phonon density of states. Band structure of $MoSi_2N_4$ monolayer after full relaxation of the crystal structure: (g) generalized gradient approximation (GGA) with the Fritz Haber Institute pseudopotential method, and (h) GGA with the optimized norm-conserving Vanderbilt pseudopotential method.

belongs to the $P6m1$ space group. Monolayer $MoSi_2N_4$ is composed of seven layers of N-Si-N-Mo-N-Si-N, which can be viewed as a MoN_2 layer sandwiched by two Si-N bilayers, with N atoms surround the Si atom, forming a polyhedral linkage between Si-N tetrahedra and Mo-N trigonal prisms. Each unit cell contains one Mo atom, two Si atoms, and four N atoms. As we know, the band structure is a crucial theoretical basis of intrinsic material properties and potential applications. Therefore, accurately describing the band structure of semiconductor materials is essential for predicting their potential applications in devices. To precisely predict $MoSi_2N_4$ device behaviors, here we first use experimental data to screen for accurate calculation methods. A recent experimental study showed that the lattice constant and band gap for $MoSi_2N_4$ are 2.94 Å and 1.94 eV, respectively [30]. Previous investigations found that the GGA-PBE-optimized $MoSi_2N_4$ unit cell is a semiconductor with a lattice constant of 2.909 Å and an indirect band gap of 1.744 eV (PBE) or 2.297 eV (HSE) [30]. Obviously, there is a difference between calculated and experimental results. To obtain highly consistent results for calculation, we consider three different exchange-correlation functions—local density approximation (LDA) Perdew-Zunge (PZ) [55], GGA PBE [49], and HSE06 [56]—combined with five different pseudopotentials—FHI [57], Hartwigsen-Goedecker-Hutter [58], OpenOMX (OMX) [59], PseudoDojo [60], and optimized norm-conserving Vanderbilt (SG15) [61]. These form 15 different calculation methods that are used to compute the lattice constant and band gap of $MoSi_2N_4$, as shown in Fig. 1(d). From Fig. 1(d), it is observed that the lattice constant and band gap calculated by the GGA-SG15 method are 2.908 Å and 1.738 eV, respectively, highly consistent with the previous theoretical report [30]. However, compared to experimental results [30], the GGA-SG15 calculation underestimates the lattice constant of $MoSi_2N_4$ and severely underestimates the band gap.

Considering that the GGA-SG15 method cannot provide accurate theoretical support for experiments, we must find the most suitable theoretical calculation that is closest to the experiment among the other 14 methods. As shown in Fig. 1(d), the GGA-OMX-calculated result is closest to the experimental lattice constant, while the GGA-FHI result is closest to the experimental band gap. However, using different calculation methods to study different characteristics of $MoSi_2N_4$ is highly unacceptable. Therefore, by detailed comparison, we find the GGA-FHI calculation method is the preferred one for accurately describing both lattice constant and band gap for $MoSi_2N_4$. How can we understand why the GGA-FHI calculation is the most suitable one for $MoSi_2N_4$? Previous studies have shown that the band-edge states of $MoSi_2N_4$ have excellent robustness and are mainly contributed by the *d* orbitals of the inner Mo atoms [62]. Therefore, its electronic structure may be affected by strong electron-electron interactions and spin-orbit coupling (SOC). To address these issues, Figs. S1 and S2 in

the Supplemental Material [63] show the strong correlation effect of *d* electrons of the Mo atom and the SOC effect on the band structure of $MoSi_2N_4$. It can be observed that considering the Hubbard *U* effect would produce results contrary to experimental data, while the introduction of the SOC effect has almost no effect on its electronic properties. As a result, the electronic structure of $MoSi_2N_4$ is strongly affected by quantum confinement, which causes significant changes in the electron density between its interior and surface, resulting in the GGA functional being closer to the experimental values than the LDA and HSE06 functional. In addition, the FHI functional is better able to capture the large variation of the electron density of the *d* orbital of Mo atoms, while the PBE functional is more likely to ignore this effect. Therefore, the GGA-FHI method has a significant advantage in describing the electronic properties of $MoSi_2N_4$.

The phonon spectrum and phonon density of states calculated by the GGA-FHI method are shown in Figs. 1(e) and 1(f). The absence of imaginary frequencies across the entire Brillouin zone confirms the dynamic stability of the $MoSi_2N_4$ monolayer. Additionally, to ensure the accurate prediction of the $MoSi_2N_4$ band gap and the correct description of its *E*-*k* dispersion relationship by the GGA-FHI method, we calculate the band structure using both GGA-FHI and GGA-SG15 methods, as depicted in Figs. 1(g) and 1(h), respectively. Notably, besides the difference in the band gap, the overall *E*-*k* dispersion relationships are highly consistent between the two calculation methods. As metallic states around the Fermi level are continuously distributed, accurately calculating the $MoSi_2N_4$ band gap can reasonably reflect the characteristics of the metal/$MoSi_2N_4$ contact. To further identify whether the GGA-FHI method can also better describe the electronic features of metal/$MoSi_2N_4$ heterojunctions, we make comparative calculations using the GGA-FHI, GGA-SG15, and higher-precision HSE-FHI methods, respectively, as shown in Figs. S3–S5 in the Supplemental Material [63]. Only slight differences can be found in the band gap of the projected band structure of the $MoSi_2N_4$ monolayer among the three methods, and the dispersion relationship of the GGA-FHI calculation is similar to those of the other two methods. However, as stated previously, the GGA-FHI method has the advantage in describing $MoSi_2N_4$, and has the lowest computational cost for investigating metal/$MoSi_2N_4$ heterojunctions. Consequently, in the subsequent investigation, we only employ the GGA-FHI method for calculations.

B. Construction and electronic structure of metal/$MoSi_2N_4$ heterojunctions

In nanoelectronic devices, it is highly desirable to choose an appropriate metal for the electrodes to inject carriers into semiconducting channel materials. To design $MoSi_2N_4$-based nanoelectronic devices, here we consider 13 different bulk metals (Sc, Bi, Ag, Al, Ti, Cr, Fe, Cu, Co, Au, Pd, Ni, and Pt) with work functions (WFs) falling in the range of 3.5–5.65 eV, giving a work function interval $\Delta WF = 2.15$ eV, and 2D semimetallic graphene (Gr) as candidate electrodes and explore the contact characteristics of the metal/$MoSi_2N_4$ interfaces. The wide WF range is selected because the continuous variation of metal WFs within the $MoSi_2N_4$ band gap is valuable for discovering contact trends. Previous studies have shown that using six layers of metal atoms is sufficient to characterize a real metal substrate [64]. Therefore, we simulate metal electrodes by using this number of layers.

To avoid the impact of strain on the electronic properties of the semiconductor $MoSi_2N_4$, we apply strain only to the metal by using the generalized lattice match (GLM) method [65], which automatically searches for all possible interface supercells based on their overall crystal structures. As shown in Figs. 2(a) and 2(b), the vectors μ_1 and μ_2 are used to define the surface cell of the bulk metal, with $\mu_{1(2)} = [\mu_{1x(2x)}, \mu_{1y(2y)}]^T$, and the vectors v_1 and v_2 are used to define the surface cell of the $MoSi_2N_4$ monolayer, with $v_{1(2)} = [v_{1x(2x)}, v_{1y(2y)}]^T$. The linear equations between $[\mu_1, \mu_2]$ and $[v_1, v_2]$ are written as follows:

$$\begin{bmatrix} A_{11} & A_{12} \\ A_{21} & A_{22} \end{bmatrix} \begin{bmatrix} u_{1x} & u_{2x} \\ u_{1y} & u_{2y} \end{bmatrix} = \begin{bmatrix} v_{1x} & v_{2x} \\ v_{1y} & v_{2y} \end{bmatrix}, \quad (3)$$

where $A = PU$ is the affine transformation matrix, *P* is a positive definite symmetric matrix defining the 2D strain tensor that deforms one cell into another, and *U* is the

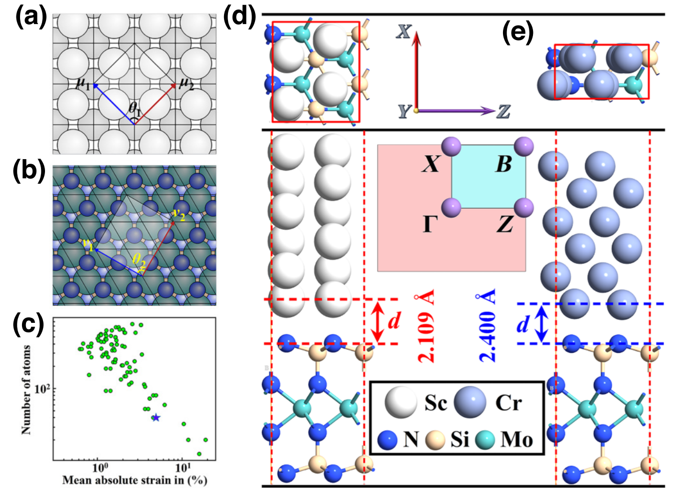

FIG. 2. The surface supercells chosen for constructing the Sc/$MoSi_2N_4$ heterojunction: (a) Sc, (b) $MoSi_2N_4$. (c) The average absolute strain versus the total number of atoms in different matching unit cells when constructing the Sc/$MoSi_2N_4$ heterojunction using the generalized lattice match method. (d) Top and side views of the Sc/$MoSi_2N_4$ heterojunction. (e) Top and side views of the Cr/$MoSi_2N_4$ heterojunction.

rotation matrix.

$$U = \begin{bmatrix} \cos(\theta) & -\sin(\theta) \\ \sin(\theta) & \cos(\theta) \end{bmatrix}, \quad (4)$$

$$P = \begin{bmatrix} 1+\varepsilon_{xx} & \varepsilon_{xy} \\ \varepsilon_{xy} & 1+\varepsilon_{yy} \end{bmatrix}, \quad (5)$$

$$\theta = |\theta_1 - \theta_2|/2, \quad (6)$$

$$P = U^T A, \quad (7)$$

where θ_1 (θ_2) is the angle between vectors μ_1 and μ_2 (v_1 and v_2). To achieve structural stability and minimize computational costs, an appropriate matching method is sought to balance the average absolute strain (ε^{av}) and the total number of atoms in the metal/$MoSi_2N_4$ heterojunction unit cell. $\varepsilon^{av} = (\varepsilon_{11} + \varepsilon_{22} + \varepsilon_{12})/3$ can be obtained from the strain tensor calculation [65], where ε_{11}, ε_{22}, and ε_{12} are the components of the strain tensor. As stated previously, we apply a small strain on metals to construct heterojunction unit cells. To further find the strain influence on their electronic structures, we calculate the band structures of various metals with and without strain, as shown in Figs. S6 and S7 in the Supplemental Material [63], respectively. It is evident that their band structures are almost the same for strained and unstrained metals. That is, the electronic properties of metals used for constructing the heterojunctions are perfectly preserved even if a small strain is applied.

When using the GLM method to construct metal/$MoSi_2N_4$ heterojunctions, the metal crystal orientation, two-monolayer adaptation supercell, and metal WF used are given in Table I. The interface models of Sc/$MoSi_2N_4$ and Cr/$MoSi_2N_4$ heterojunctions after sufficient relaxation are presented in Figs. 2(d) and 2(e). The equilibrium average interlayer distances for these two heterojunctions are 2.109 and 2.400 Å, respectively, indicating strong interlayer hybridization, which is favorable for the formation of a low Schottky barrier, or even the occurrence of Ohmic contact. The stacking configurations of the other metal/$MoSi_2N_4$ heterojunctions are shown in Fig. S8 in the Supplemental Material [63]. Figures 3(a)–3(i) exhibit the lattice constants, angles between two basis vectors, interlayer twist angles, total number of atoms per unit cell, interface area, sum of covalent radii of nearest interface atoms, average interlayer distance, average absolute strain, and binding energy for all metal/$MoSi_2N_4$ heterojunctions. In particular, Figs. 3(a)–3(g) provide the matching information for the heterojunction constructions, and Fig. 3(h) shows the sum of covalent radii (d_R) and equilibrium interlayer distance (d_M) after full relaxation of the heterojunctions. Generally, this quantity can characterize the degree of interface hybridization: if d_R is close to d_M, then there is a strong hybridization. Clearly, Sc, Ti, Cr, Fe, Co, Pd, and Pt/$MoSi_2N_4$ heterojunctions have similar values for d_R and d_M, suggesting a strong hybridization at their interfaces.

To assess the structural stability of the constructed metal/$MoSi_2N_4$ heterojunctions, we calculate the interface binding energy using

$$E_b = (E_H - E_M - E_{MoSi_2N_4})/n_{MoSi_2N_4}, \quad (8)$$

where E_H, E_M, and $E_{MoSi_2N_4}$ are the total energies of the metal/$MoSi_2N_4$ heterojunction, isolated metal layer, and $MoSi_2N_4$ monolayer, respectively. $n_{MoSi_2N_4}$ is the total number of atoms in the $MoSi_2N_4$ layer of the heterojunction. From Fig. 3(i), it can be seen that the binding energies for all metal/$MoSi_2N_4$ heterojunctions are negative, indicating the energy lowers during the formation of the heterojunctions, thus they are energetically stable. The differences among these binding energies are mainly related to the d_M and the intrinsic physical properties of the metals. For instance, Gr/$MoSi_2N_4$ has the largest interlayer distance (3.27 Å) due to the dominance of van der Waals forces, resulting in the smallest absolute value of binding energy. On the other hand, Pt/$MoSi_2N_4$, which has a smaller interlayer distance and two unpaired electrons [Pt ($5d^9 6s^1$)], exhibits a strong interface interaction, making it the heterojunction with the largest absolute value of binding energy. Similar trends have been detected in other metal-semiconductor heterojunctions [66–70] (Table I).

Figures 4(a) and 4(f) show the projected band structures for Sc/$MoSi_2N_4$ and Cr/$MoSi_2N_4$ heterojunctions, where the red and blue denote the band structures

TABLE I. The metal crystal orientations, matched crystal lattices, and metal work functions for the construction of metal/$MoSi_2N_4$ heterojunctions.

	Sc(100)	Bi(111)	Ag(100)	Al(100)	Ti(100)	Graphene	Cr(100)
Metal	$\sqrt{2}\times\sqrt{2}$	$\sqrt{3}\times\sqrt{3}$	2×1	2×1	3×1	2×2	2×1
$MoSi_2N_4$	$\sqrt{3}\times2$	$\sqrt{7}\times\sqrt{7}$	$\sqrt{3}\times1$	$\sqrt{3}\times1$	$2\sqrt{3}\times1$	$\sqrt{3}\times\sqrt{3}$	$\sqrt{3}\times1$
WF (eV)	3.5	4.22	4.26	4.28	4.33	4.45	4.5
	Fe(100)	Cu(110)	Co(100)	Au(100)	Pd(100)	Ni(100)	Pt(100)
Metal	4×2	2×1	$\sqrt{3}\times\sqrt{3}$	$\sqrt{3}\times1$	2×1	$\sqrt{5}\times\sqrt{5}$	2×1
$MoSi_2N_4$	$4\times\sqrt{3}$	$\sqrt{3}\times1$	$2\times\sqrt{3}$	$\sqrt{3}\times1$	$\sqrt{3}\times1$	$2\times\sqrt{3}$	$\sqrt{3}\times1$
WF (eV)	4.5	4.65	5	5.1	5.12	5.15	5.65

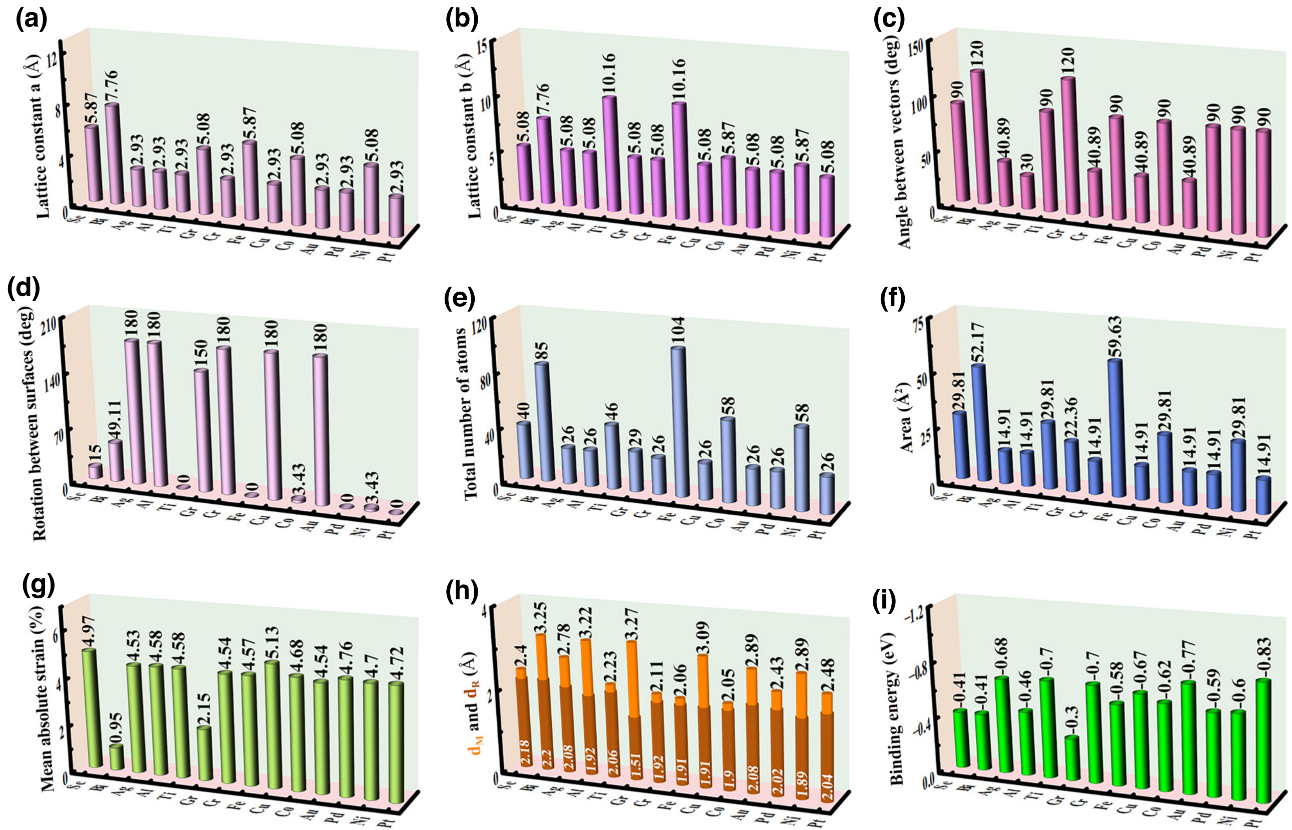

FIG. 3. Using the generalized lattice match method to construct the metal/$MoSi_2N_4$ heterojunction: (a) lattice constant in the *a* direction, (b) lattice constant in the *b* direction, (c) angle between lattice vectors, (d) interlayer rotation angle, (e) total number of atoms, (f) interface area, (g) average absolute strain, (h) the sum of covalent radii of interface atoms (d_R) and equilibrium interlayer distance (d_M), and (i) binding energy.

projected onto $MoSi_2N_4$, and the line width represents the weight. Compared with the isolated monolayer, the $MoSi_2N_4$ band structure in the metal/$MoSi_2N_4$ system possesses a significant hybridization with the metal band structure. In the Sc/$MoSi_2N_4$ heterojunction, the projected $MoSi_2N_4$ bands cross the Fermi level, indicating the formation of chemical bonds at the interface, resulting in the metallization of $MoSi_2N_4$. Similar phenomena are found in other metal/$MoSi_2N_4$ systems, as shown in Fig. S3 in the Supplemental Material [63]. Ti/$MoSi_2N_4$, Fe/$MoSi_2N_4$, and Co/$MoSi_2N_4$ exhibit a strongest hybridization, while Bi/$MoSi_2N_4$, Al/$MoSi_2N_4$, Gr/$MoSi_2N_4$, and Cu/$MoSi_2N_4$ show a weaker hybridization, and others fall in between. In short, the degree of band hybridization is closely related to the equilibrium interlayer distance in the metal/$MoSi_2N_4$ system: a smaller interlayer distance corresponds to a larger orbital overlap and greater hybridization. In strongly bonded systems, *d*-orbital electrons dominate most of the bands, while *s*- and *p*-orbital electrons contribute mainly in weakly bonded systems [69].

As stated previously, the disruption of the $MoSi_2N_4$ band structure suggests the presence of chemical bonds between $MoSi_2N_4$ and the metals. To further confirm this point, we calculate the density of states projected onto the $MoSi_2N_4$ layer for metal/$MoSi_2N_4$ heterojunctions, as shown in Figs. 4(b) and 4(g). Clearly, the metallized Sc/$MoSi_2N_4$ has a higher density of states near the Fermi level compared with the nonmetallized Cr/$MoSi_2N_4$. Figure S9 in the Supplemental Material [63] also shows that the strongly bonded systems have a large density of states within the $MoSi_2N_4$ band gap, a typical signature of metallization, indicating the presence of metal-induced gap states (MIGS). Additionally, the carrier-doping capability of the metal can be measured by calculating the lowest valence electron density (LVED) at the metal/$MoSi_2N_4$ interface. From Figs. 4(c) and 4(h), it can be seen that Cr/$MoSi_2N_4$ has a higher LVED than Sc/$MoSi_2N_4$, suggesting that the former can form a lower contact resistance. The LVEDs for the remaining contact systems are provided in Fig. S10 in the Supplemental Material [63]. Generally, strongly bonded systems correspond to a high absolute value of binding energy, band hybridization, density of states, and LVED. Most of the systems in our study can fit well to this trend. However, the LVEDs of Cr/$MoSi_2N_4$ and Sc/$MoSi_2N_4$ are exceptions.

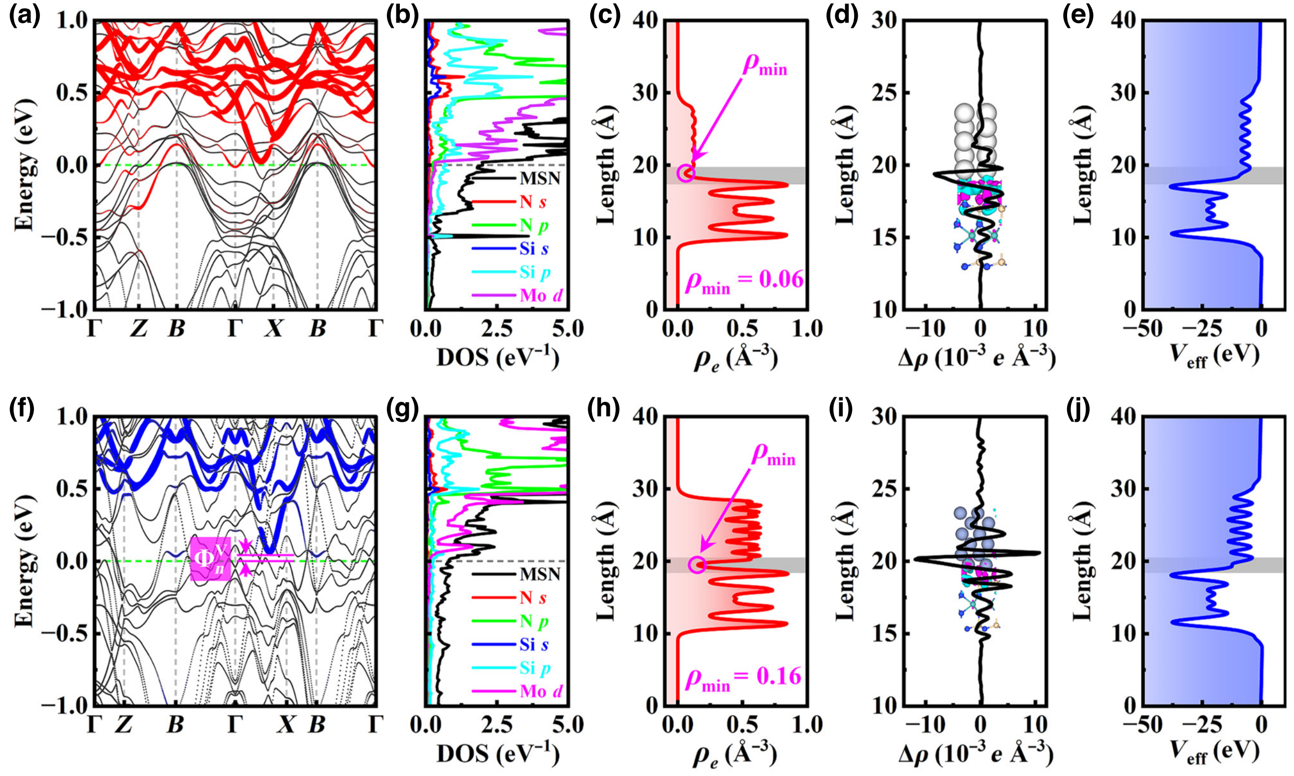

FIG. 4. For the Sc/$MoSi_2N_4$ heterojunction: (a) the projected band structure, (b) the projected density of states (PDOS) of the $MoSi_2N_4$ layer, (c) the valence electron density, (d) the planar average charge density difference, and (e) the effective potential. For the Cr/$MoSi_2N_4$ heterojunction: (f) the projected band structure, (g) the PDOS of the $MoSi_2N_4$ layer, (h) the valence electron density, (i) the planar average charge density difference, and (j) the effective potential. MSN in figure (b) and figure (g) is the abbreviation of $MoSi_2N_4$.

This is because Sc ($3d^1 4s^2$) lacks electrons in the *d* orbital, resulting in minimal orbital overlap, while Cr ($3d^5 4s^1$) is rich in electrons in the *d* orbital, allowing more extensive orbital overlap at the interface.

Owing to interlayer binding, charge redistribution occurs, leading to the flow of electrons from one layer with a higher work function to another layer with a lower work function. This process results in the accumulation of two opposite-polarity net charges at the interface, establishing a built-in electric field. To visually present the charge transfer characteristics at the metal/$MoSi_2N_4$ interface, we calculate the space-charge-density difference using

$$\Delta\rho(x,y,z) = \rho_{\text{metal/MSN}}(x,y,z) - \rho_{\text{metal}}(x,y,z) - \rho_{\text{MSN}}(x,y,z), \quad (9)$$

and we calculate the average charge-density difference along the *z*-direction, defined by

$$\Delta\rho(z) = \int \rho_{\text{metal/MSN}}(x,y,z)dxdy - \int \rho_{\text{metal}}(x,y,z)dxdy - \int \rho_{\text{MSN}}(x,y,z)dxdy, \quad (10)$$

where $\rho_{\text{Metal/MSN}}$, ρ_{Metal}, and ρ_{MSN} are the charge densities of the metal/$MoSi_2N_4$ system, isolated metal, and $MoSi_2N_4$ at the (*x,y,z*) point. The positive and negative values in the one-dimensional charge density difference denote electron accumulation and depletion, while the pink and cyan colors in the three-dimensional charge density difference similarly indicate electron accumulation and depletion. As shown in Figs. 4(d), 4(i), and S11 in the Supplemental Material [63], the charge redistribution at all metal/$MoSi_2N_4$ interfaces is asymmetric, indicating that interlayer charge transfer leads to the generation of an interface electric dipole moment. The local built-in electric field caused by this interface dipole moment penetrates into the $MoSi_2N_4$, resulting in an overall shift of its band structure and alteration of the interface potential distribution, ultimately lowering the dependence of the interface SBH on the metal work function [71].

To determine the position and shape of the tunneling barrier (TB) and to quantify the efficiency of charge injection in metal/$MoSi_2N_4$ systems, we calculate the effective potential for each metal/$MoSi_2N_4$ system, as shown in Fig. S12(a) in the Supplemental Material [63]. The size of the TB can be characterized by its height (Φ_{TB}) and width (W_{TB}). A high and wide TB makes it difficult for

electrons to cross the interface vacuum gap, thus reducing the electron tunneling probability. However, a small and narrow TB often corresponds to a stronger orbital overlap, enhancing carrier tunneling. From Figs. 4(e) and 4(j), it can be seen that the Sc/$MoSi_2N_4$ system has no TB due to the metallization of $MoSi_2N_4$, while the Cr/$MoSi_2N_4$ system forms a very small TB owing to a strong interlayer coupling. The effective potentials for other metal/$MoSi_2N_4$ systems are given in Fig. S12 in the Supplemental Material [63], and the interlayer tunneling probability (P_{TB}) can be computed as follows:

$$P_{TB} = \exp\left(-\frac{2\sqrt{2m\Phi_{TB}}}{\hbar}W_{TB}\right), \tag{11}$$

where m and $\hbar$ are the effective mass of free electrons and the reduced Planck constant, respectively. From Figs. 5(a)–5(c), it can be seen that 100% carrier injection from Sc, Ag, Ti, Pd, and Pt into $MoSi_2N_4$ can be achieved, while it is almost completely blocked by the vacuum gap for Bi-, Al-, Gr-, and Ni-based systems, because the efficiency of carrier injection is closely related to the system's lattice coherence and orbital overlap [72].

C. Interface electrical contact property of metal/$MoSi_2N_4$ heterojunctions

To obtain metal electrodes with a low contact resistance for 2D nanoelectronic devices, we must consider not only the injection efficiency of charge carriers (P_{TB}) but also the combined effects of interface contact barrier and channel transport barrier ($\Phi^{C}_{n,p}$). As shown in Fig. 6(a), the interface contact barriers can be further divided into vertical Schottky barrier ($\Phi^{V}_{n,p}$) and horizontal Schottky barrier ($\Phi^{h}_{n,p}$). Here, $\Phi^{V}_{n,p}$ represents the barrier between the metal electrode region A and the semiconductor region B, which can be evaluated by the difference between the Fermi level and the conduction band minimum (CBM) or valence band maximum (VBM) of the $MoSi_2N_4$ projected band structure in the metal/$MoSi_2N_4$ system (Schottky-Mott rule [73]), as illustrated in Figs. 4(f) and S3(f) in the Supplemental Material [63]. $\Phi^{h}_{n,p}$ is the barrier occurring at the coupling interface between the electrode region ($A+B$) and the channel region C to lower the efficiency of carrier transport, which can be quantified by transmission gaps above or below the Fermi level (the positive or negative energy region) in the transmission spectra, as shown in Figs. 6(b) and 6(e). $\Phi^{C}_{n,p}$ is the carrier transport barrier in the channel material, which can be determined by projecting the

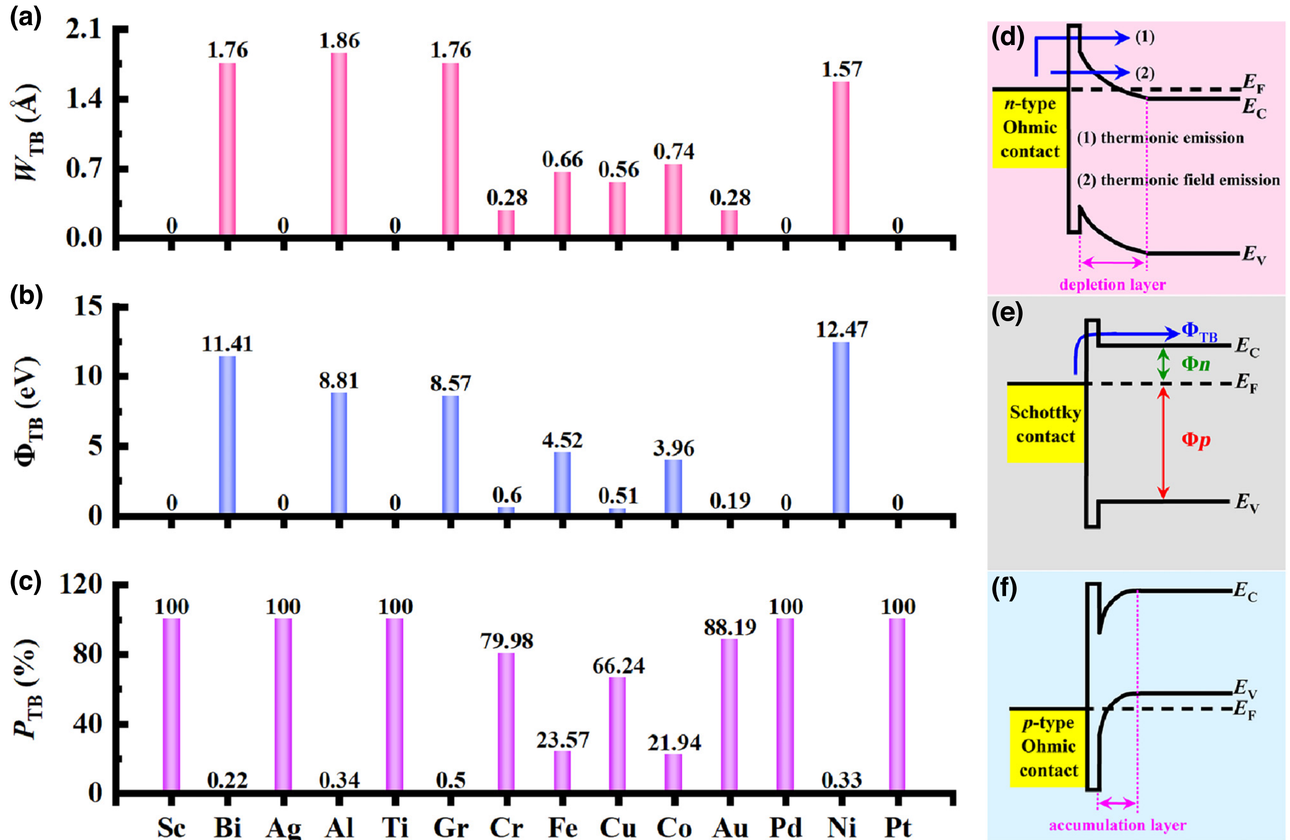

FIG. 5. The (a) width and (b) height of the tunneling barrier, and the (c) tunneling probability. Schematic representations of contact types: (d) n-type Ohmic contact, (e) Schottky contact, and (f) p-type Ohmic contact.

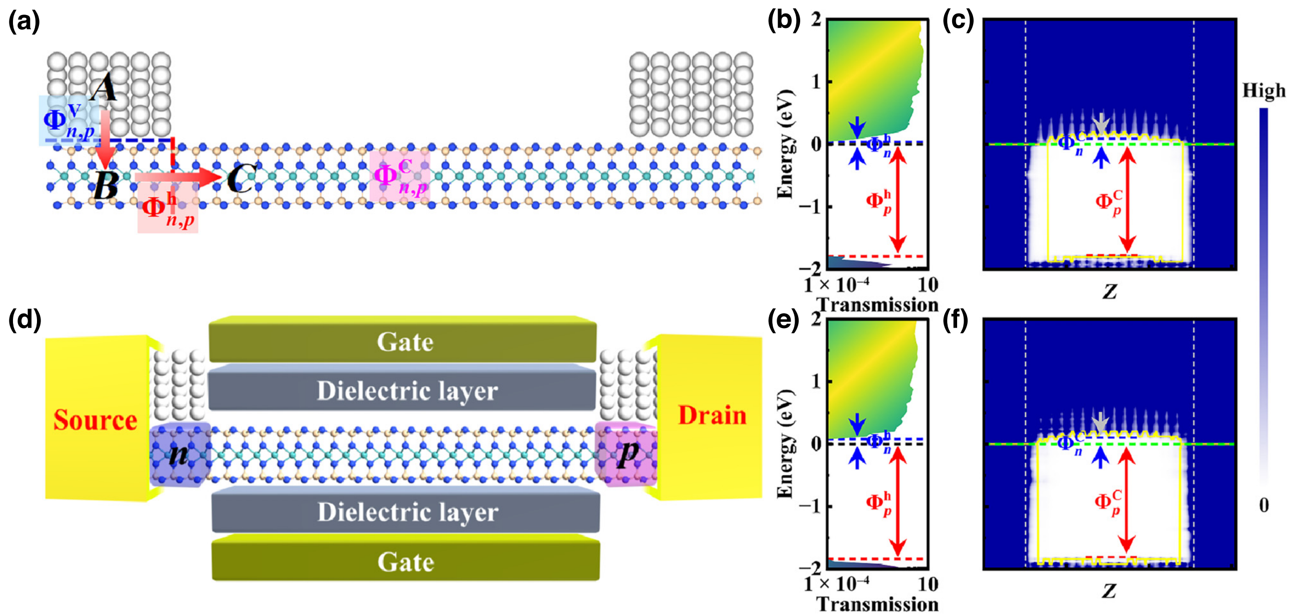

FIG. 6. (a) Illustration for the various interface contact barrier. For the $Sc/MoSi_2N_4$ field-effect transistor (FET): (b) transmission spectra, and (c) projected local density of states (PLDOS). (d) A schematic diagram of the 5.1-nm FET. For the $Cr/MoSi_2N_4$ FET: (e) transmission spectra and (f) PLDOS.

CBM and VBM of the channel material into real space visually by the PLDOS, as shown in Figs. 6(c) and 6(f), where the absolute values of positive and negative barriers are referred to as the n- and p-type barriers, respectively. In short, n-type barriers in a device can be classified as n-type vertical Schottky barriers (Φ_n^V), n-type horizontal Schottky barriers (Φ_n^h), and n-type channel transport barriers (Φ_n^C). Similarly, three types of p-type barriers occur in a device, which are abbreviated as Φ_p^V, Φ_p^h, and Φ_p^C.

As is well known, the construction of HP FETs is closely related to the SBH. A lower SBH can significantly reduce carrier scattering, thereby improving transistor performance and benefiting a high ON-state current and high-frequency operation of FETs. Therefore, investigating the SBH of FETs is of great significance. The presence of FLP hinders the adjustment of the SBH by changing the work function, making all metal/$MoSi_2N_4$ contacts ultimately form one of the contact types shown in Figs. 5(d)–5(f). The strong interlayer charge transfer and orbital hybridization lead to metallization of the $MoSi_2N_4$ in the electrode coverage area, as shown in Figs. 5(d) and 5(f), resulting in the disappearance of n- and p-type barriers and the formation of n- and p-type Ohmic contacts. The formation of Ohmic contacts implies the disappearance of barriers during carrier transport, giving rise to a linear current-voltage relationship, which is ideal for device transport. However, due to the presence of surface states [73], MIGS [74], and other factors, it is difficult to achieve true Ohmic contacts in practical electronic devices. Obviously, the SBH is the main factor limiting contact resistance, and Schottky contacts, as shown in Fig. 5(e), are generally the norm for all kinds of electronic devices.

As mentioned earlier, the bulk metal/$MoSi_2N_4$ interface will undergo strong FLP due to the influence of interface chemical bonds, charge transfer, interface dipoles, and MIGS. This will cause the SBH predicted by the Schottky-Mott rule [73] to deviate from experimental measurements significantly. Fortunately, the SBH obtained by quantum transport simulation shows a good consistency with already-existing experimental results. This is because the FET is considered as a whole; that is, this method fully accounts for the coupling between the metal and the semiconductor (characterized by $\Phi_{n,p}^V$) as well as the interface coupling between the entire device electrode and the channel material section (characterized by $\Phi_{n,p}^h$). On the other hand, the projected band structure calculation treats the electrode and channel materials separately, making them less reliable due to excluding $\Phi_{n,p}^h$. To obtain a more accurate SBH, possibly agreeing with experiments, we construct a quantum transport simulation device model, as shown in Fig. 6(d). The electrode and channel parts of the device are composed of metal/$MoSi_2N_4$ heterojunctions and an intrinsic $MoSi_2N_4$ monolayer, respectively. According to the 2013 ITRS requirements [46] for a 5.1-nm HP transistor in 2028, the gate length, equivalent oxide thickness, and relative dielectric constant of the device should be 5.1 nm, 0.41 nm, and 3.9, respectively. It is noted that the electron mobility of the $MoSi_2N_4$ monolayer along the zigzag (287.79 cm^2 V^{-1} s^{-1}) and armchair (261.96 cm^2 V^{-1} s^{-1}) directions is basically

similar [30]. However, our calculations show that, compared with the zigzag direction, the device transport along the armchair direction can lower computational cost significantly. Therefore, we choose the armchair-type FET for the quantum transport simulation. Using the calculated transmission spectra and PLDOS at zero bias and zero gate bias, as displayed in Figs. 6(b), 6(e), and S13 in the Supplemental Material [63], and Figs. 6(c), 6(f), and S14 in the Supplemental Material [63], respectively, we can extract the SBH values for all metal/$MoSi_2N_4$ systems, and these SBHs are labeled in the corresponding figures.

In order to compare these SBHs obtained from the Schottky-Mott rule [73] and quantum transport simulation visually, we summarize various Schottky barriers ($\Phi^{V}_{n,p}$, $\Phi^{h}_{n,p}$, and $\Phi^{C}_{n,p}$) derived from the projected band structure (PBS), transmission spectra (TS), and PLDOS in Figs. 7(a) and 7(b). From the SBH obtained by the transport simulation, it can be seen that, except for Gr/$MoSi_2N_4$ forming a p-type Schottky contact, all other metal/$MoSi_2N_4$ systems exhibit n-type Schottky contacts. This result indicates that FETs constructed from the 13 types of bulk metal/$MoSi_2N_4$ heterojunctions are all n-type FETs. As shown in Fig. 7(a), for the SBHs in most of the systems, Φ^{V}_{n} are smaller than Φ^{h}_{n} and Φ^{C}_{n}, but Φ^{h}_{n} are similar to Φ^{C}_{n}. A similar conclusion has also been drawn in other theoretical studies [64,75]. It should be noted that experimental measurements have shown that the theoretically calculated values of Φ^{V}_{n} and Φ^{h}_{n} always underestimate the actual SBH, and may even mistakenly classify the contact type as Ohmic. In contrast, the quantum transport simulation can not only accurately predict the contact type, but also provide SBH values very close to experimental results [76]. Therefore, in the subsequent part for the selection of suitable metal electrodes, we tend to focus on the Φ^{C}_{n} value. Additionally, the strength of the FLP can be quantitatively described by the pinning factor S, defined as $S = d\Phi_{SB}/dM_{WF}$, where Φ_{SB} and M_{WF} are the Schottky barrier height and metal work function, respectively. If $S = 0$, it indicates a complete FLP, and $S = 1$, it means the absence of FLP, completely following the Schottky-Mott rule [73]. The corresponding S values obtained by linearly fitting the n-type SBH as a function of metal work function are shown in Figs. 7(c)–7(e). It is worth mentioning that, for Gr/$MoSi_2N_4$, no dangling bonds exist on the 2D material surfaces and the presence of vdW gaps significantly weakens the FLP, and that the Gr/$MoSi_2N_4$ forms a p-type Schottky contact, as stated previously; therefore, Gr/$MoSi_2N_4$ is not included in the fitting calculation. The fitting result shows that the order of FLP strength is PBS(0.37) > TS(0.23) > PLDOS(0.17). Considering that the quantum transport simulations are closer to experiments, such a result implies that there is a stronger FLP at the bulk metal/$MoSi_2N_4$ interface, which is consistent with the previous analysis.

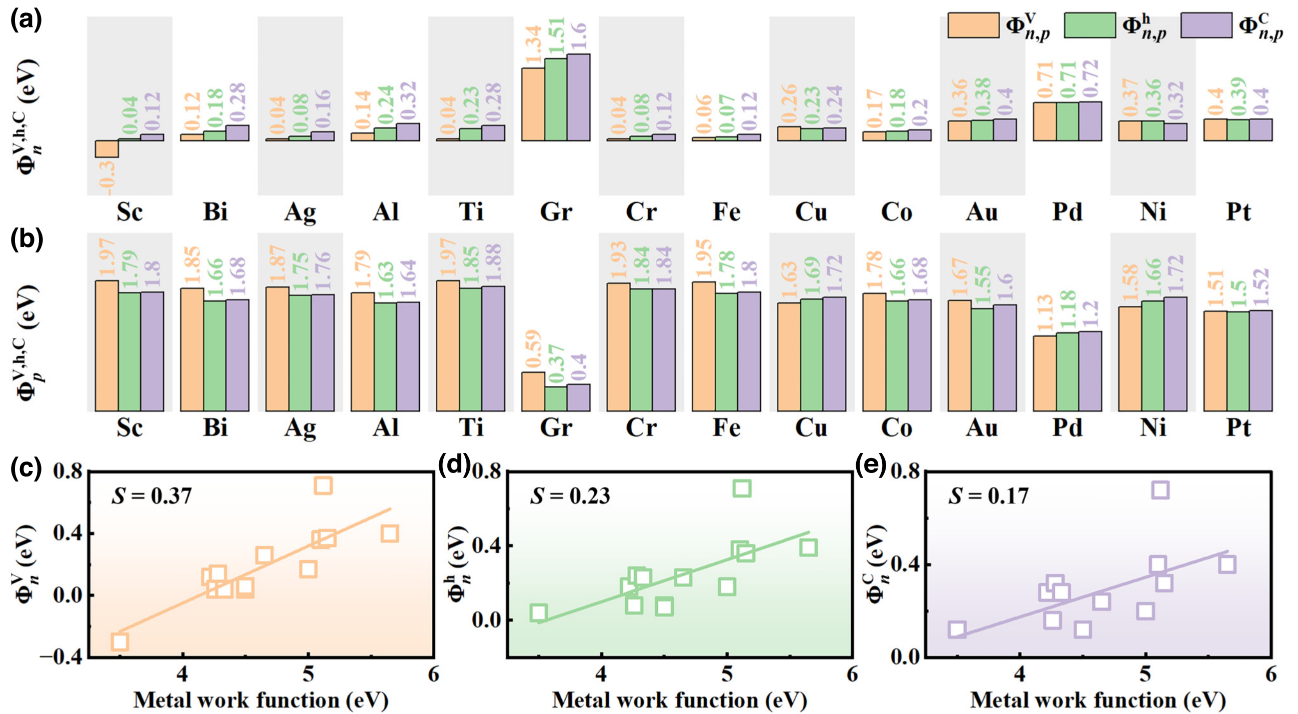

FIG. 7. Based on three different methods including projected band structure, transmission spectra, and projected density of states, two types of Schottky barrier height (SBH) are obtained: (a) n-type SBH and (b) p-type SBH. The pinning factors for the three different types of n-type SBH are determined by linear fitting of (c) Φ^{V}_{n}, (d) Φ^{h}_{n}, and (e) Φ^{C}_{n}.

D. Quantum transport simulation for $MoSi_2N_4$-based 5.1-nm field-effect transistors

The presence of Schottky barriers generally leads to a larger contact resistance at the metal/$MoSi_2N_4$ interface, thereby reducing the charge transport in the device, increasing the power consumption of integrated devices, and shortening the device lifespan. Obviously, achieving a lower SBH or Ohmic contacts is crucial for designing HP $MoSi_2N_4$ devices. By comparing the SBH values obtained from quantum transport simulations, it is found that Sc/$MoSi_2N_4$, Cr/$MoSi_2N_4$, and Fe/$MoSi_2N_4$ all exhibit the lowest n-type SBH, 0.12 eV [see Fig. 7(a)]. However, the significant tunneling barrier at the Fe/$MoSi_2N_4$ interface (see Fig. 5) hinders the efficiency of electron injection from Fe to $MoSi_2N_4$. Thus, we only explore the performance of 5.1-nm FET devices consisting of $MoSi_2N_4$ as a channel material combined with Sc and Cr as electrodes. Figure 6(d) shows the structural model of the device, which is a dual-probe dual-gate device, with equal gate voltages for both gates, and its source and drain electrode temperatures are set to 300 K.

When doping the $MoSi_2N_4$ in the electrode region, the compensation charge method is used by changing the density of individual atoms to introduce additional charges [77]. The Poisson equation for the device is solved with periodic, Neumann, and Dirichlet boundary conditions applied in the x (horizontal), y (vertical), and z (transport) directions, respectively. For simplicity, the devices with Sc and Cr electrodes are referred to as $D1$ and $D2$, respectively. The ON-state current (I_{ON}) in nanoelectronic devices is an important parameter reflecting the operation speed of device. I_{ON} is defined as the current corresponding to the ON-state gate voltage $V_g(\mathrm{ON})$, representing the switching capability of the device. Here, $V_g(\mathrm{ON}) = V_g(\mathrm{OFF}) + V_{dd}$, where $V_g(\mathrm{OFF})$ is the OFF-state gate voltage corresponding to the OFF-state current I_{OFF}, and the power supply voltage V_{dd} is taken to be equal to the bias voltage V_b. According to the 2013 ITRS standard [46] for devices with nodes of 5.1 nm and below in 2028, taking $V_b = 0.64$ V, namely $V_{dd} = V_b = 0.64$ V, the required I_{OFF} and I_{ON} for HP [low-power (LP)] FETs are 0.1 μA/μm (5×10^{-5} μA/μm) and 900 μA/μm (295 μA/μm), respectively.

As shown in Fig. 8(a), when we use the same concentration for n-type or p-type doping for the electrode part, the transfer characteristics curves of the three types of FETs (n-i-n, p-i-p, and p-i-n) almost overlap under the same doping conditions, indicating similar performance under the same doping conditions. As a comparison, we also calculate the I-V characteristics of p-i-n junction $D1$ devices below 5.1 nm, with the same parameters and requirements (effective oxide layer thickness, bias voltage, and switching state criteria) as shown in Fig. S15 in the Supplemental Material [63]. We can see that, owing to the influence of the short-channel effect, only the 5.1-nm device is capable of simultaneously meeting the OFF-state requirements for both HP and LP FETs. Therefore, we choose only the 5.1-nm p-i-n FET including n-type and p-type doping cases for further study. From Figs. 8(b) and 8(c), it can be seen that the intrinsic state (0 doping) of $D1$ and $D2$ can meet the OFF-state requirements of HP FETs, and $D1$ can meet the OFF-state requirements of LP devices but still fails to reach the ON-state standards for both HP and LP devices. Therefore, we attempt to improve the device performance by using different doping concentrations and a high-k (H-k) gate dielectric layer.

As shown in Figs. 8(b) and 8(c), the $MoSi_2N_4$ part of the device's electrode is doped with concentrations of 10^{16}, 10^{18}, 10^{19}, 10^{20}, and 10^{21} e/cm^3 to study the effect of doping concentration on the performance of $D1$ and $D2$ (p-i-n FET) devices. To present these results more clearly, the V_{OFF}, V_{ON}, and I_{ON} extracted from the transmission characteristic curves are summarized and plotted in Figs. 8(d)–8(i). Prominently, all doped devices can meet the OFF-state requirement of HP FETs, but none of them can reach the ON-state standard. As shown in Fig. 8(d), compared to HP $D1$, HP $D2$ appears more robust upon V_{OFF}. Moreover, at a doping concentration of 10^{21} e/cm^3, the direction of V_{OFF} for HP $D1$ is reversed, indicating that the direction of V_{OFF} for HP $D1$ can be switched by using different doping concentrations. Unfortunately, the device performance for all doped devices is worst at the doping concentration of 10^{21} e/cm^3 [see Figs. 8(b) and 8(c)]. The possible reason for this result is that the excessive doping leads to the localization of electronic states, introducing a large number of impurity scattering centers, and increasing the scattering of electrons in the lattice. Figure 8(e) shows that, influenced by V_{OFF}, the V_{ON} of HP $D1$ is always higher than that of $D2$ in the entire doping range, indicating that HP $D1$ will have a larger I_{ON} with a larger V_{ON}, which is confirmed in Fig. 8(f).

I_{ON} is a key parameter reflecting the operation speed of the device. If traditional Si is used as the dielectric layer, the doping would reduce the I_{ON} of HP $D1$. When the doping concentration is taken as 10^{16} and 10^{18} e/cm^3, the I_{ON} of HP $D2$ is almost unaffected. Although I_{ON} increases slightly as doping concentration increases further, this effect is weak. Therefore, we consider replacing the low-k (L-k) Si ($\varepsilon = 3.9$) dielectric layer with a H-k HfO_2 ($\varepsilon = 25$) dielectric layer to improve device performance. It is found that for the undoped HP $D1$ and HP $D2$ devices, V_{OFF} (V_{ON}) decreases (increases) by using H-k. For the HP $D1$ device with a doping concentration of 10^{20} e/cm^3, V_{OFF} (V_{ON}) increases (decreases), but the opposite change occurs for the HP $D2$ device [i.e., V_{OFF} (V_{ON}) decreases (increases)]. As shown in Fig. 8(f), for undoped HP $D1$ (HP $D2$) devices, using H-k directly reduces (increases) I_{ON}, but under the doping concentration of 10^{20} e/cm^3

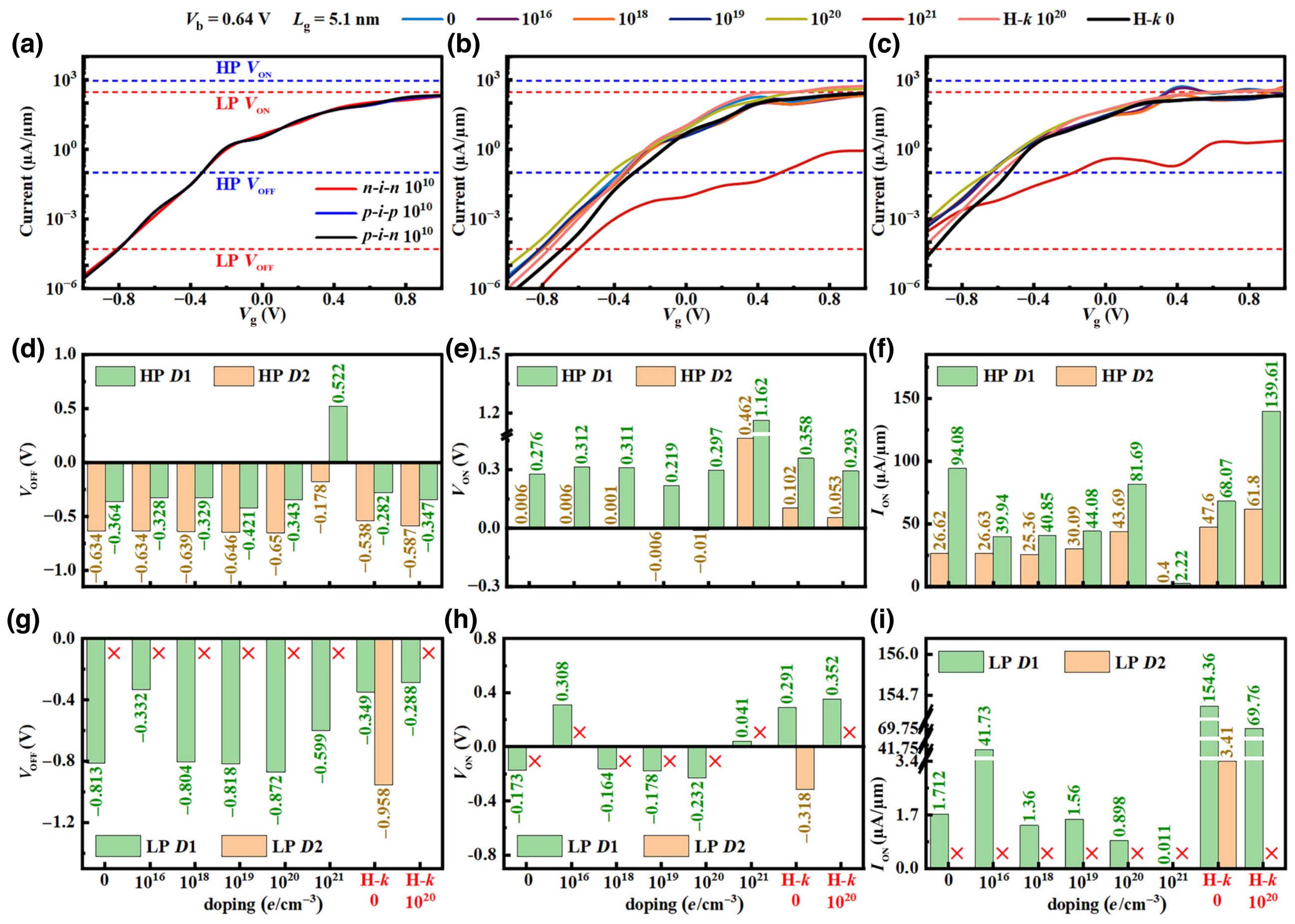

FIG. 8. (a) Under same doping conditions (10^{10} e/cm^3), transfer characteristics curves for *n-i-n*, *p-i-p*, and *p-i-n* junction FETs. For *p-i-n* FETs, transfer characteristic curves are illustrated under various doping concentrations or high-*k* gate effects for (b) *D*1 and (c) *D*2. Under different doping concentrations or the high-*k* gate effects: (d),(g) OFF-state voltage (V_{OFF}); (e),(h) ON-state voltage (V_{ON}); and (f),(i) ON-state current (I_{ON}) for high-performance (HP) *D*1, low power (LP) *D*1, HP *D*2, and LP *D*2 devices.

combining with H-*k*, the I_{ON} of HP *D*1 (HP *D*2) can be increased by 48.4% (132.2%). Although the improvement in I_{ON} is more significant for the HP *D*2 device, it still lags HP *D*1 after enhancement. In addition, for the application of FETs, the ON:OFF current ratio ($I_{\mathrm{ON}}/I_{\mathrm{OFF}}$) is another important quality factor. From Fig. 8(f), it can be seen that under the combination of a doping concentration of 10^{20} e/cm^3 and H-*k*, both devices achieve the maximum ON:OFF ratio (approximately 1.4×10^3). Compared to undoped devices, the ON:OFF ratio of HP *D*1 is increased by one order of magnitude.

Now, we study the performance of *D*1 and *D*2 in LP FETs. From Figs. 8(b) and 8(c), as can be seen, all doped or H-*k* conditions of LP *D*1 can meet the OFF-state requirements in the studied gate voltage range (−1.0 to 1.0 V), but only the undoped H-*k* device of LP *D*2 can meet the OFF-state requirements. As shown in Fig. 8(g), the OFF-state voltage of LP *D*1 without doping and with doping concentrations ranging from 10^{18} to 10^{20} e/cm^3 is too high for the OFF-state criterion, and the introduction of an H-*k* gate helps to reduce the OFF-state voltage of LP *D*1. By definition, V_{ON} changes inversely with V_{OFF}, as shown in Fig. 8(h). From Fig. 8(i), it can be seen that using H-*k* can significantly improve the I_{ON} and ON:OFF ratio of LP *D*1. For example, the undoped and 10^{20}-e/cm^3-doped LP *D*1 devices increase I_{ON} by 2 orders of magnitude and achieve an ON:OFF ratio as high as 3×10^6 under the combination of 10^{20}-e/cm^3 doping and H-*k*. The undoped LP *D*1 device, after using H-*k*, can meet 52.33% of the ITRS requirement for the LP FET ON-state current. It is worth noting that, without using H-*k*, the ON-state current of the LP *D*1 device with a doping concentration of 10^{16} e/cm^3 is 24 times larger than that of the undoped device. Unfortunately, as shown in Fig. S16(b) in the Supplemental Material [63], although the device using H-*k* can improve HP *D*1 to some extent, it significantly increases (decreases) the OFF-state (ON-state) voltage of LP *D*1, directly leading to the weakening of I_{ON}.

In short, under different doping concentrations and/or H-*k* conditions, device performance is significantly changed. All doped HP devices can meet the OFF-state standards of ITRS, and under the combination of

10^{20}-e/cm^3 doping and H-k, the I_{ON} of HP $D1$ and HP $D2$ is increased by 48.4% and 132.2%, respectively. LP $D1$ can meet the OFF-state requirement under different doping conditions. However, for LP $D2$, only the undoped H-k device can meet the OFF-state requirement. Using H-k can significantly improve the I_{ON} and ON:OFF ratio for LP $D1$, where undoped and 10^{20}-e/cm^3-doped LP $D1$ devices achieve I_{ON} increasing by 2 orders of magnitude, with an ON:OFF ratio as high as 3×10^6. Considering the 13 kinds of bulk metals under study, the bulk metal Sc is the most suitable as the electrodes for $MoSi_2N_4$ FETs. Therefore, the optimization strategy proposed in this work provides an alternative avenue for designing HP and LP $MoSi_2N_4$-based devices.

To explain the physical origin of doping concentration and H-k gate effects on the current of devices, in Fig. 9, we take HP $D1$ as an example and display the transmission spectra, PLDOS, and the transmission eigenstates at $E = 1.0$ eV at the Γ point for doping concentrations of 0 and 10^{20} e/cm^3, and the corresponding H-k device under the conditions of $V_b = 0.64$ V and $V_g = 0.0$ V. From the transmission spectrum, it can be seen that devices with high current density often correspond to larger transmission coefficients and transmission spectra closer to the Fermi level of the left electrode (E_L) [see Figs. 9(a) and 9(g)]. Similarly, for higher current densities, there are more electronic states occurring in the conduction and valence bands of the PLDOS [see Figs. 9(b) and 9(h)]. In Figs. 9(i)–9(l), we also present the transmission eigenstates of the device at $E = 1.0$ eV at the Γ point, representing the scattering states of electrons from the source electrode (left electrode) to the drain electrode (right electrode). Transmission eigenstates with larger amplitudes distributed in the scattering region reflect a higher transmission probability of the incident states from the source electrode through the channel region to the

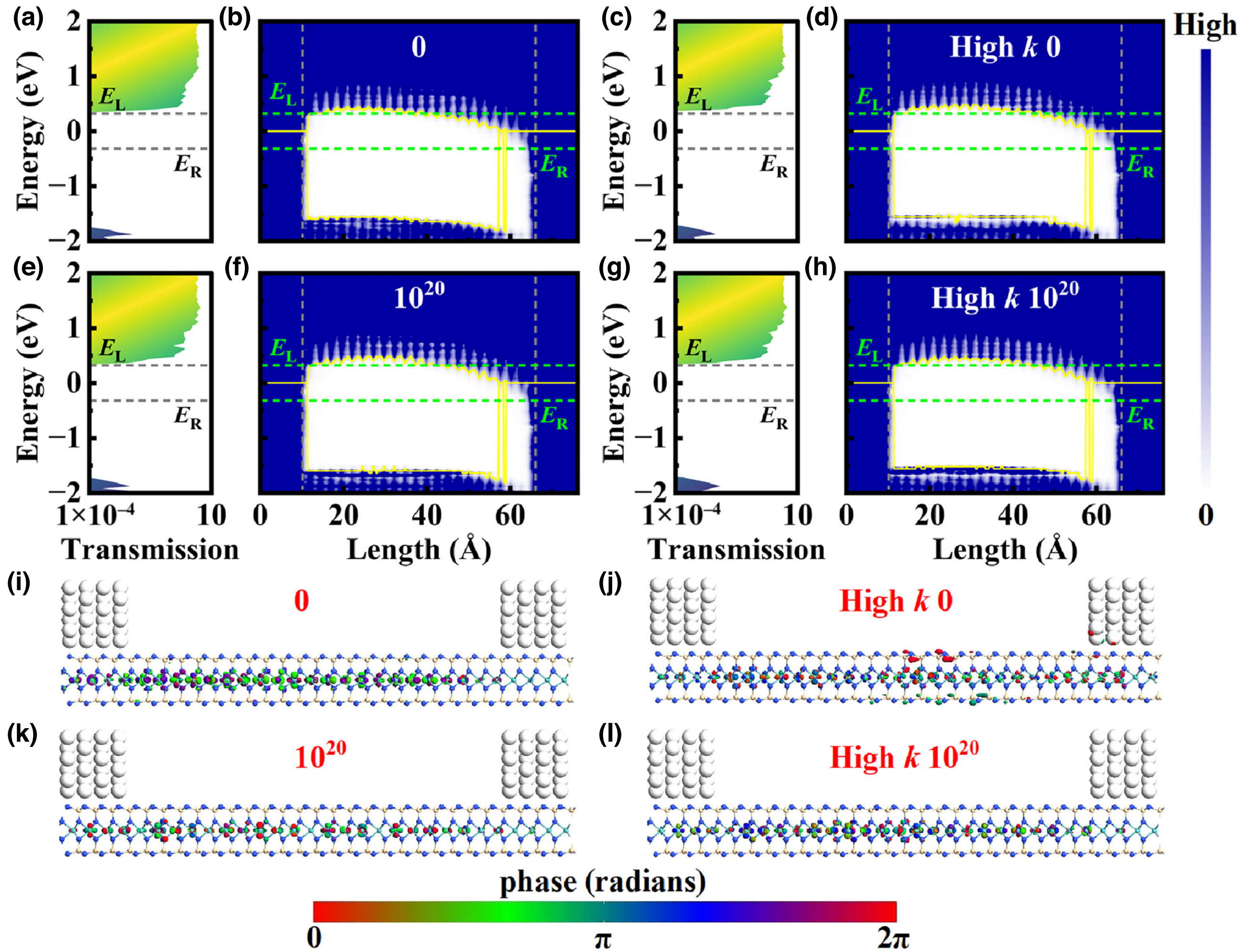

FIG. 9. (a),(c) [(e),(g)] Transmission spectrum; (b),(d) [(f),(h)] projected local density of states (PLDOS); and (i),(j) [(k),(l)] the transmission eigenstates at $E = 1.0$ eV at the Γ point with an isosurface of 0.4 for the undoped (doping concentration 10^{20} e/cm^3) high-performance (HP) $D1$ device by using low-k (L-k) and high-k (H-k) at $V_b = 0.64$ V and $V_g = 0.0$ V. E_L and E_R represent the Fermi levels of the left and right electrodes, respectively.

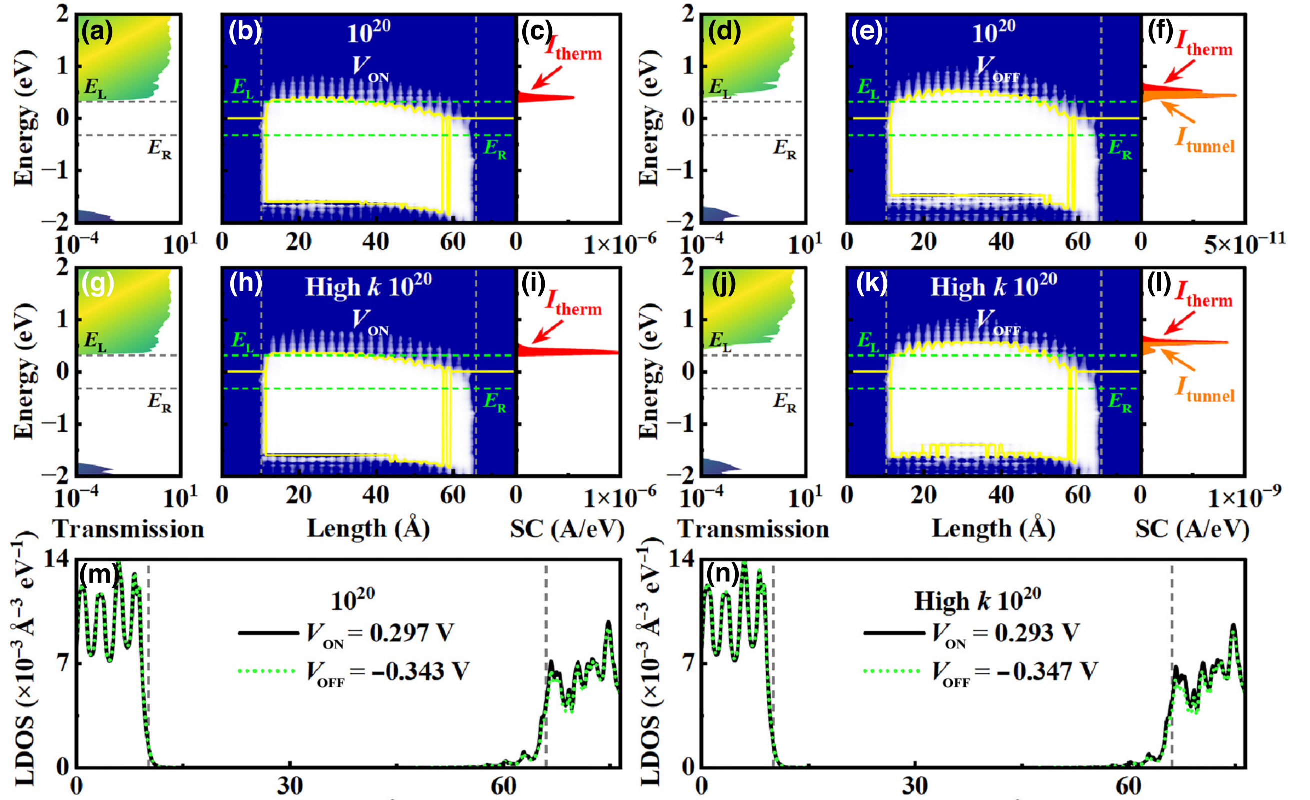

FIG. 10. For the high-performance (HP) $D1$ device under doping conditions of 10^{20} e/cm^3: (a),(d) transmission spectra, (b),(e) projected local density of states (PLDOS), (c),(f) spectral current (SC), and (m) local density of states (LDOS) for the ON and OFF states. The combination of 10^{20} e/cm^3 doping and a high-k gate effects: (g),(j) transmission spectra, (h),(k) PLDOS, (i),(l) spectral current, and (n) LDOS for the ON and OFF states. E_L and E_R represent the Fermi levels of the left and right electrodes, respectively.

drain electrode. In particular, we can see that the H-k gate device with a doping concentration of 10^{20} e/cm^3 exhibits transmission eigenstates with a broader distribution range and larger amplitudes than the undoped high-k gate device or the device with a doping concentration of 10^{20} e/cm^3, corresponding to their different current densities.

Furthermore, we analyze the transmission spectra, PLDOS, spectral current, and LDOS of the HP $D1$ device with a doping concentration of 10^{20} e/cm^3 and the H-k gate device in the ON and OFF state. As mentioned earlier, when HP $D1$ is in the ON state with a high current density, its transmission spectrum is larger and closer to E_L. From the PLDOS, it can be observed that the transport gap is larger in the OFF state compared to the ON state, which is manifested in the different Φ_n^C [see Figs. 10(b) and 10(e) or Figs. 10(h) and 10(k)]. Additionally, the high-k gate effect can increase the ON-state current, caused by the higher electronic density in the channel region, facilitating carrier transport. The spectral current calculations reveal that the ON-state current is contributed by thermionic emission, while the OFF-state current is primarily attributed to the tunneling current. The ON-state spectral current of the HP $D1$ device with a doping concentration of 10^{20} e/cm^3 and the H-k device is higher by 5 and 3 orders of magnitude, respectively, as shown in Figs. 10(c), 10(f), 10(i), and 10(l). As exhibited in Figs. 10(b) and 10(e) or Figs. 10(h) and 10(k), the ON and OFF state of devices can be switched by the gate-voltage-induced bending of the energy bands of the channel region. Additionally, we calculate the LDOS of the device, as shown in Figs. 10(m) and 10(n). Clearly, the density of states on the right side of the device in the ON state is always higher than that in the OFF state. Therefore, whether the device conducts depends on the positive gate voltage corresponding to the ON-state current, similar to electron doping, leading to a decrease in the barrier Φ_n^C and, in turn, an increase in the transmission coefficient, and thus the injection of more electrons. Additionally, owing to the occurrence of a high electronic density of states near E_L, even with a slight reduction in the channel barrier under H-k or gate voltage control, a sudden increase in current can be achieved, in contrast with the situation of the OFF state for devices.

IV. CONCLUSIONS

In summary, based on the experimental data, we determine the most suitable calculation method among 15 different combinations of computational methods and

identify the GGA-FHI calculation to be the most accurate approach to describe the band gap and lattice constant for the $MoSi_2N_4$ monolayer. The interface characteristics for 13 different bulk metals and 2D-semimetal graphene in contact with the semiconductor $MoSi_2N_4$ monolayer are investigated systematically by calculating binding energy, projected band structure, $MoSi_2N_4$ projected density of states, valence electron density, plane-averaged charge density difference, effective potential, and SBH. It is found that there exists the significant MIGS at the bulk metal/$MoSi_2N_4$ interfaces, thus leading to different degrees of metallization for $MoSi_2N_4$. The Sc, Ag, Ti, Pd, and Pt electrodes can achieve 100% carrier injection, and the *n*-type Schottky contact occurs for all bulk metal/$MoSi_2N_4$ interfaces, while the graphene/$MoSi_2N_4$ interface exhibits the *p*-type Schottky contact.

By quantum transport simulations, which can accurately predict experimental results, a pinning factor of 0.17 for the bulk metal/$MoSi_2N_4$ interface is obtained, showing a strong FLP effect at the metal/$MoSi_2N_4$ interface. Compared with quantum transport simulations, the SBH is generally underestimated by Schottky-Mott rule. Calculations for the transport characteristics of $D1$ and $D2$ devices indicate that the application of optimization strategies by doping or using a H-k gate can substantially enhance device performance. In particular, HP $D1$, HP $D2$, and LP $D1$ can meet ITRS standards of the related FET in the OFF state. However, in the studied gate voltage range, only the LP $D2$ with the H-k strategy for the undoped device can meet ITRS requirement of the LP FET in the OFF state. For HP $D1$ with an electrode with doping concentration of 10^{20} e/cm^3, the ON-state current is increased by an order of magnitude when the H-k gate is used, achieving an ON:OFF ratio of 1.4×10^3. Similarly, the undoped LP $D1$ with H-k optimization exhibits a 2-order-of-magnitude increase in ON-state current, reaching an ON:OFF ratio of 3×10^6. These results suggest that Sc is the best bulk metal to serve as the electrodes with $MoSi_2N_4$ as a channel material to construct FETs. Additionally, we elucidate the physical origins influencing device performance by the calculated transmission spectra, PLDOS, spectral current, and LDOS. Our study not only increases the understanding of the interaction mechanisms of metal/$MoSi_2N_4$ interfaces, but also provides a theoretical reference for selecting suitable metals for the electrodes of $MoSi_2N_4$-based nanoelectronic devices, and opening an alternative avenue to optimize device performance.

ACKNOWLEDGMENTS

This work is supported by the National Natural Science Foundation of China (Grant No. 61771076), and Postgraduate Scientific Research Innovation Project of Hunan Province, China (Grant No. CX20220957).

[1] M. Chhowalla, D. Jena, and H. Zhang, Two-dimensional semiconductors for transistors, Nat. Rev. Mater. **1**, 16052 (2016).

[2] Y. Wang and Manish Chhowalla, Making clean electrical contacts on 2D transition metal dichalcogenides, Nat. Rev. Phys. **4**, 101 (2022).

[3] A. Dimoulas, P. Tsipas, A. Sotiropoulos, and E. K. Evangelou, Fermi-level pinning and charge neutrality level in germanium, Appl. Phys. Lett. **89**, 25 (2006).

[4] X. C. Liu, M. S. Choi, E. Hwang, W. J. Yoo, and J. Sun, Fermi level pinning dependent 2D semiconductor devices: Challenges and prospects, Adv. Mater. **34**, 2108425 (2022).

[5] H. Pan, L. M. Tang, and K. Q. Chen, Quantum mechanical modeling of magnon-phonon scattering heat transport across three dimensional ferromagnetic/nonmagnetic interfaces, Phys. Rev. B **105**, 064401 (2022).

[6] Z. K. Ding, Y. J. Zeng, H. Pan, N. N. Luo, J. Zeng, L. M. Tang, and K. Q. Chen, Edge states of topological acoustic phonons in graphene zigzag nanoribbons, Phys. Rev. B **106**, L121401 (2022).

[7] H. Pan, Z. K. Ding, B. W. Zeng, N. N. Luo, J. Zeng, L. M. Tang, and K. Q. Chen, *Ab initio* Boltzmann approach to coupled magnon phonon thermal transport in ferromagnetic crystals, Phys. Rev. B **107**, 104303 (2023).

[8] Y. H. Jung, M. S. Choi, A. Nipane, A. Borah, B. Kim, A. Zangiabadi, T. Taniguchi, K. Watanabe, W. J. Yoo, J. Hone, and J. T. Teherani, Transferred via contacts as a platform for ideal two-dimensional transistors, Nat, Electron. **2**, 187 (2019).

[9] A. S. Aji, P. Solá¡ůs-Fernández, H. G. Ji, K. Gukuda, and H. Ago, High mobility WS_2 transistors realized by multilayer graphene electrodes and application to high responsivity flexible photodetectors, Adv. Funct. Mater. **27**, 1703448 (2017).

[10] N. A. N. Phan, H. Noh, J. Kim, Y. Kim, H. Kim, D. Whang, N. Aoki, K. Watanabe, T. Taniguchi, and G. H. Kim, Enhanced performance of WS_2 field-effect transistor through mono and bilayer h-BN tunneling contacts, Small **18**, 2105753 (2022).

[11] X. L. Liu, C. Zhang, E. L. Li, C. F. Gao, R. X. Wang, Y. Liu, F. C. Liu, W. Shi, Y. H. Yuan, J. Sun, Y. F. Lin, J. H. Chu, and W. W. Li, Ultralow off-state current and multilevel resistance state in van der Waals heterostructure memristors, Adv. Funct. Mater. **22**, 2309642 (2023).

[12] J. L. Wang, Q. Yao, C. W. Huang, X. M. Zou, L. Liao, S. S. Chen, Z. Y. Fan, K. Zhang, W. Wu, X. H. Xiao, C. Z. Jiang, and W. W. Wu, High mobility MoS_2 transistor with low Schottky barrier contact by using atomic thick h-BN as a tunneling layer, Adv. Mater. **28**, 8302 (2016).

[13] L. M. Yang, K. Majumdar, H. Liu, Y. C. Du, H. Wu, M. Hatzistergos, P. Y. Hung, R. Tieckelmann, W. Tsai, C. Hobbs, and P. D. Ye, Chloride molecular doping technique on 2D materials: WS_2 and MoS_2, Nano Lett. **14**, 6275 (2014).

[14] S. Das, H. Y. Chen, A. V. Penumatcha, and J. Appenzeller, High performance multilayer MoS_2 transistors with scandium contacts, Nano Lett. **13**, 100 (2013).

[15] R. Kappera, D. Voiry, S. E. Yalcin, B. Branch, G. Gupta, A. D. Mohite, and M. Chhowalla, Phase-engineered low-resistance contacts for ultrathin MoS_2 transistors, Nat. Mater. **13**, 1128 (2014).

[16] G. Kwon, Y. H. Choi, H. Lee, H. S. Kim, J. Jeong, K. Jeong, M. Baik, H. Kwon, J. Ahn, E. Lee, and M. H. Cho, Interaction-and defect-free van der Waals contacts between metals and two-dimensional semiconductors, Nat. Electron. **5**, 241 (2022).

[17] J. K. Xiao, K. L. Chen, X. K. Zhang, X. Z. Liu, H. H. Yu, L. Gao, M. Y. Hong, L. Gu, Z. Zhang, and Y. Zhang, Approaching Ohmic contacts for ideal monolayer MoS_2 transistors through sulfur-vacancy engineering, Small Methods **7**, 2300611 (2023).

[18] R. S. Chen, G. L. Ding, Y. Zhou, and S. T. Han, Fermi-level depinning of 2D transition metal dichalcogenide transistors, J. Mater. Chem. C **9**, 11407 (2021).

[19] Y. Wang, J. C. Kim, Y. Li, K. Y. Ma, S. Hong, M. Kim, H. S. Shin, H. Y. Jeong, and M. Chhowalla, P-type electrical contacts for 2D transition-metal dichalcogenides, Nature **610**, 61 (2022).

[20] Y. Wang, J. C. Kim, R. J. Wu, J. Martinez, X. Song, J. Yang, F. Zhao, A. Mkhoyan, H. Y. Jeong, and M. Chhowalla, Van der Waals contacts between three-dimensional metals and two-dimensional semiconductors, Nature **568**, 70 (2019).

[21] W. Y. Li, Q. Y. Tao, Z. W. Li, G. H. Yang, Z. Y. Lu, Y. Chen, Y. Wen, Y. L. Wang, L. Liao, Y. Liu, and J. He, Monolayer black phosphorus and germanium arsenide transistors via van der Waals channel thinning, Nat. Electron. **1**, 1854 (2023).

[22] W. D. Wang, *et al.*, Clean assembly of van der Waals heterostructures using silicon nitride membranes, Nat. Electron. **1**, 4978 (2023).

[23] Z. J. Zhou, F. C. Hou, X. Huang, G. Wang, Z. H. Fu, W. L. Liu, G. W. Yuan, J. Xu, J. H. Lin, and L. Gao, Stack growth of wafer-scale van der Waals superconductor heterostructures, Nature **621**, 499 (2023).

[24] S. Gamage, Z. Li, V. S. Yakovlev, C. Lewis, H. Wang, S. B. Cronin, and Y. Abate, Nanoscopy of black phosphorus degradation, Adv. Mater. Interfaces **3**, 1600121 (2016).

[25] Y. Y. Wang, R. X. Fei, R. Quhe, J. Z. Li, H. Zhang, X. Y. Zhang, B. Shi, L. Xiao, Z. G. Song, J. B. Yang, J. Shi, F. Pan, and J. Lu, Many-body effect and device performance limit of monolayer InSe, ACS Appl. Mater. Interfaces **10**, 23344 (2018).

[26] S. Ross and A. Sussman, Surface oxidation of molybdenum disulfide, J. Phys. Chem. **59**, 889 (1955).

[27] Y. Y. Wang, P. Huang, M. Ye, R. Quhe, Y. Y. Pan, H. Zhang, H. X. Zhong, J. J. Shi, and J. Lu, Many-body effect, carrier mobility, and device performance of hexagonal arsenene and antimonene, Chem. Mater. **29**, 2191 (2017).

[28] X. T. Sun, Z. G. Song, S. Q. Liu, Y. Y. Wang, Y. Y. Li, W. Z. Wang, and J. Lu, Sub-5 nm monolayer arsenene and antimonene transistors, ACS Appl. Mater. Interfaces **10**, 22363 (2018).

[29] J. H. Yan, H. Pang, L. Xu, J. Yang, R. Quhe, X. Y. Zhang, Y. Y. Pan, B. W. Shi, S. Q. Liu, L. Q. Xu, J. B. Yang, F. Pan, Z. Y. Zhang, and J. Lu, Excellent device performance of sub-5-nm monolayer tellurene transistors, Adv. Electron. Mater. **5**, 1900226 (2019).

[30] Y. L. Hong, Z. B. Liu, L. Wang, T. Y. Zhou, W. Ma, C. Xu, S.n Feng, L. Chen, M. L. Chen, D. M. Sun, X. Q. Chen, H. M. Cheng, and W. C. Ren, Chemical vapor deposition of layered two-dimensional $MoSi_2N_4$ materials, Science **369**, 670 (2020).

[31] L. M. Cao, G. H. Zhou, Q. Q. Wang, L. K. Ang, and Y. S. Ang, Two-dimensional van der Waals electrical contact to monolayer $MoSi_2N_4$, Appl. Phys. Lett. **118**, 013106 (2021).

[32] A. Bafekry, M. Faraji, D. M. Hoat, M. Shahrokhi, M. M. Fadlallah, F. Shojaei, S. A. H. Feghhi, M. Ghergherehchi, and D. Gogova, $MoSi_2N_4$ single-layer: A novel two-dimensional material with outstanding mechanical, thermal, electronic and optical properties, J. Phys. D: Appl. Phys. **54**, 155303 (2021).

[33] B. Mortazavi, B. Javvaji, F. Shojaei, T. Rabczuk, A. V. Shapeev, and X. Y. Zhuang, Exceptional piezoelectricity, high thermal conductivity and stiffness and promising photocatalysis in two-dimensional $MoSi_2N_4$ family confirmed by first-principles, Nano Energy **82**, 105716 (2021).

[34] C. C. Jian, X. C. Ma, J. Q. Zhang, and X. Yong, Strained $MoSi_2N_4$ monolayers with excellent solar energy absorption and carrier transport properties, J. Phys. Chem. C **125**, 15185 (2021).

[35] Q. Q. Wang, L. M. Cao, S. J. Liang, W. K. Wu, G. Z. Wang, C. H. Lee, W. L. Ong, H. Y. Yang, L. K. Ang, S. A. Yang, and Y. S. Ang, Efficient Ohmic contacts and built-in atomic sublayer protection in $MoSi_2N_4$ and WSi_2N_4 monolayers, npj 2D Mater. Appl. **5**, 71 (2021).

[36] K. Nandan, B. Ghosh, A. Agarwal, S. Bhowmick, and Y. S. Chauhan, Two-dimensional $MoSi_2N_4$: An excellent 2D semiconductor for field-effect transistors, IEEE Trans. Electron Devices **69**, 406 (2021).

[37] R. Islam, B. Ghosh, C. Autieri, S. Chowdhury, A. Bansil, A. Agarwal, and B. Singh, Tunable spin polarization and electronic structure of bottom-up synthesized $MoSi_2N_4$ materials, Phys. Rev. B **104**, L201112 (2021).

[38] M. Kong, S. Murakami, and T. Zhang, A comprehensive study of complex non-adiabatic exciton dynamics in $MoSi_2N_4$, Mater. Today Phys. **27**, 100814 (2022).

[39] Y. Q. Cai, G. Zhang, and Y. W. Zhang, Polarity-reversed robust carrier mobility in monolayer MoS_2 nanoribbons, J. Am. Chem. Soc. **136**, 6269 (2014).

[40] Z. H. Li, J. N. Han, S. G. Cao, and Z. H. Zhang, $NbS_2/MoSi_2P_4$ van der Waals heterojunction: Flexibly tunable electrical contact properties and potential applications for Schottky junction devices, Appl. Surf. Sci. **636**, 157766 (2023).

[41] Z. H. Li, J. N. Han, S. G. Cao, and Z. H. Zhang, Graphene/$MoSi_2X_4$: A class of van der Waals heterojunctions with unique mechanical and optical properties and controllable electrical contacts, Appl. Surf. Sci. **614**, 156095 (2023).

[42] X. He, Z. Gao, Z. H. Zhang, K. Xiong, and Y. He, Simulation studies on robust contacts in $V_2CT_2/MoSi_2N_4$ (T = O, F, OH) van der Waals heterojunction nanostructures: Implications for optoelectronic devices, ACS Appl. Nano Mater. **6**, 18337 (2023).

[43] J. Huang, P. Li, X. Ren, and Z. X. Guo, Promising properties of a sub-5-nm monolayer $MoSi_2N_4$ transistor, Phys. Rev. Appl. **16**, 044022 (2021).

[44] X. T. Sun, Z. G. Song, N. N. Huo, S. Q. Liu, C. Yang, J. Yang, W. Z. Wang, and J. Lu, Performance limit of monolayer $MoSi_2N_4$ transistors, J. Mater. Chem. C **9**, 14683 (2021).

[45] K. Nandan, S. Bhowmick, Y. S. Chauhan, and A. Agarwal, Designing power-efficient transistors using

narrow-bandwidth materials from the MA_2Z_4 (M = Mo, Cr, Zr, Ti, Hf; A = Si, Ge; Z = N, P, As) monolayer series, Phys. Rev. Appl. **19**, 064058 (2023).
[46] International Technology Roadmap for Semiconductors (ITRS) (2017), http://www.itrs2.net/2013-itrs.html
[47] M. Brandbyge, J. L. Mozos, P. Ordejón, J. Taylor, and K. Stokbro, Density-functional method for nonequilibrium electron transport, Phys. Rev. B **6**, 5165401 (2002).
[48] S. Smidstrup, *et al.*, QuantumATK: An integrated platform of electronic and atomic-scale modelling tools, J. Phys.: Condens. Matter **32**, 015901 (2019).
[49] J. P. Perdew, K. Burke, and M. Ernzerhof, Generalized gradient approximation made simple, Phys. Rev. Lett. **77**, 3865 (1996).
[50] J. R. Chelikowsky and S. G. Louie, First-principles linear combination of atomic orbitals method for the cohesive and structural properties of solids: Application to diamond, Phys. Rev. B **29**, 3470 (1984).
[51] V. Blum, R. Gehrke, F. Hanke, P. Havu, V. Havu, X. Ren, K. Reuter, and M. Scheffler, Ab initio molecular simulations with numeric atom-centered orbitals, Comput. Phys. Commun. **180**, 2175 (2009).
[52] H. J. Monkhorst and J. D. Pack, Special points for Brillouin-zone integrations, Phys. Rev. B **13**, 5188 (1976).
[53] S. Grimme, J. Antony, S. Ehrlich, and H. Krieg, A consistent and accurate ab initio parametrization of density functional dispersion correction (DFT-D) for the 94 elements H-Pu, J. Chem. Phys. **132**, 154104 (2010).
[54] D. Çakır and F. M. Peeters, Dependence of the electronic and transport properties of metal-$MoSe_2$ interfaces on contact structures, Phys. Rev. B **89**, 245403 (2014).
[55] W. Kohn and L. J. Sham, Self-consistent equations including exchange and correlation effects, Phys. Rev. **140**, A1133 (1965).
[56] M. Marsman, J. Paier, A. Stroppa, and G. Kresse, Hybrid functionals applied to extended systems, J. Phys.: Condens. Matter **20**, 064201 (2008).
[57] M. Fuchs and M. Scheffler, Ab initio pseudopotentials for electronic structure calculations of poly-atomic systems using density-functional theory, Comput. Phys. Commun. **119**, 67 (1999).
[58] S. Goedecker, M. Teter, and J. Hutter, Separable dual-space Gaussian pseudopotentials, Phys. Rev. B **54**, 1703 (1996).
[59] T. Ozaki, Variationally optimized atomic orbitals for large-scale electronic structures, Phys. Rev. B **67**, 155108 (2003).
[60] M. J. van Setten, M. Giantomassi, E. Bousquet, M. J. Verstraete, D. R. Hamann, X. Gonze, and G. M. Rignanese, The PseudoDojo: Training and grading a 85 element optimized norm-conserving pseudopotential table, Comput. Phys. Commun. **226**, 39 (2018).
[61] M. Schlipf and F. Gygi, Optimization algorithm for the generation of ONCV pseudopotentials, Comput. Phys. Commun. **196**, 36 (2015).
[62] Y. B. Wu, Z. Tang, W. Y. Xia, W. W. Gao, F. H. Jia, Y. B. Zhang, W. G. Zhu, W. Q. Zhang, and P. H. Zhang, Prediction of protected band edge states and dielectric tunable quasiparticle and excitonic properties of monolayer $MoSi_2N_4$, NPJ Comput. Mater. **129**, 8 (2022).
[63] See Supplemental Material at http://link.aps.org/supplemental/10.1103/PhysRevApplied.21.054062 for additional figures in support of the data analysis.
[64] Y. Pan, Y. Wang, M. Ye, R. Quhe, H. Zhong, Z. Song, X. Peng, D. Yu, J. Yang, J. Shi, and J. Lu, Monolayer phosphorene-metal contacts, Chem. Mater. **28**, 2100 (2016).
[65] L. Jelver, P. M. Larsen, D. Stradi, K. Stokbro, and K. W. Jacobsen, Determination of low strain interfaces via geometric matching, Phys. Rev. B **96**, 085306 (2017).
[66] Y. Guo, F. Pan, M. Ye, X. T. Sun, Y. Y. Wang, J. Z. Li, X. Y. Zhang, H. Zhang, Y. Y. Pan, Z. G. Song, J. B. Yang, and Jing Lu, Monolayer bismuthene-metal contacts: A theoretical study, ACS Appl. Mater. Interfaces **9**, 23128 (2017).
[67] Y. Shu, Y. Q. Liu, Z. Cui, R. Xiong, Y. G. Zhang, C. Xu, J. Y. Zheng, C. L. Wen, B. Wu, and B. S. Sa, Efficient Ohmic contact in monolayer CrX_2N_4 (X = C, Si) based field-effect transistors, Adv. Electron Mater. **9**, 2201056 (2023).
[68] X. D. Zhang, L. P. Feng, S. C. Zhong, Y. M. Ye, H. X. Pan, P. F. Liu, X. Q. Zheng, H. Y. Li, M. Y. Qu, and X. T. Wang, Schottky barrier heights and mechanism of charge transfer at metal-Bi_2OS_2 interfaces, Sci. China Mater. **66**, 811 (2023).
[69] K. Jiang, C. D. Zheng, K. L. Yao, S. C. Zhu, and K. M. Wu, Interfacial electrical properties and transport properties of monolayer black AsP alloy in contact with metal, Mater. Today Commun. **31**, 103262 (2022).
[70] J. H. Yan, X. Y. Zhang, Y. Y. Pan, J. Z. Li, B. Shi, S. Q. Liu, J. Yang, Z. G. Song, H. Zhang, M. Ye, R. Quhe, Y. Y. Wang, B. Yang, F. Pan, and J. Lu, Monolayer tellurene-metal contacts, J. Mater. Chem. C **6**, 6153 (2018).
[71] Z. M. Tang, Q. H. Gong, and M. Yi, Spin-selective contact type and strong Fermi level pinning at a CrI_3/metal interface, Mater. Today Nano **22**, 100309 (2023).
[72] B. Ouyang, S. Y. Xiong, and Y. H. Jing, Tunable phase stability and contact resistance of monolayer transition metal dichalcogenides contacts with metal, NPJ 2D Mater. Appl. **2**, 13 (2018).
[73] J. Bardeen, Surface states and rectification at a metal semiconductor contact, Phys. Rev. **71**, 717 (1947).
[74] W. Mönch, Mechanisms of barrier formation in Schottky contacts: Metal-induced surface and interface states, Appl. Surf. Sci. **41**, 128 (1990).
[75] H. X. Zhong, R. Quhe, Y. Y. Wang, Z. Y. Ni, M. Ye, Z. G. Song, Y. Y. Pan, J. B. Yang, L. Yang, M. Lei, J. J. Shi, and J. Lu, Interfacial properties of monolayer and bilayer MoS_2 contacts with metals: Beyond the energy band calculations, Sci. Rep. **6**, 21786 (2016).
[76] S. Das, W. Zhang, M. Demarteau, A. Hoffmann, M. Dubey, and A. Roelofs, Tunable transport gap in phosphorene, Nano Lett. **14**, 5733 (2014).
[77] Z. H. Li, J. N. Han, S. G. Cao, Z. H. Zhang, and X. Q. Deng, Physical properties of monolayer $Mn(BiTeS)_2$ and its applications in sub-3 nm spintronic devices, Phys. Rev. B **108**, 184413 (2023).